

Theory for TERS of 2D materials including out-of-plane Raman response

Raul Corrêa,^{1,*} Luiz G. Cançado,¹ and Ado Jorio^{1,†}

¹*Departamento de Física, Universidade Federal de Minas Gerais,
Belo Horizonte, MG 30123-970, Brazil*

(Dated: May 12, 2026)

arXiv:2605.08387v1 [physics.optics] 8 May 2026

Abstract

Tip-Enhanced Raman Spectroscopy (TERS) can be used to make nanoscale spatial measurements of 2D materials, such as graphene and transition metal dichalcogenides (TMDs). The TERS theory introduced in [Phys. Rev. X **4**, 031054 (2014)], however, was tailored for graphene, whose out-of-plane Raman response is neglected. In the present work, we include the out-of-plane response in the TERS theory. In doing so, we provide an exact analytical expression for the field propagation between the tip and the sample, and show that the contribution to the TERS signal that scatters first at the sample, then at the tip (sample-tip, or TS) is important only when the out-of-plane response is significant. We extensively study the variation of TERS experimental measurements when varying physical parameters of the system, like the tip radius, the out-of-plane response, the TERS coherence length, and others. It becomes evident that the TERS enhancement is very sensitive to the out-of-plane Raman response of the phonon mode, while normalized tip-approach measurements are more sensitive to the coherence length, and we show that the medium refractive index leads to an effective tip enhancement factor f_e . Our results lead to the conclusion that, in general, a strong TERS enhancement is a necessary condition for investigating the physics discussed here, which here means surveying the difference in TERS signals between different Raman modes. We use our model to analyze some graphene TERS experiments, showing that they are consistent with a negligible out-of-plane Raman response and a non-zero TERS coherence length in the fitting.

I. INTRODUCTION

Raman spectroscopy is a powerful well-established technique to investigate physical and chemical properties of materials, in which light is scattered inelastically by interaction with material degrees of freedom, to frequencies adjacent to the excitation field [1, 2]. When exciting with visible light, these frequency changes are very small, so resolution-wise one is optically limited by the excitation wavelength, that is tenths of micrometers. In this resolution, small spatial coherences in the electric polarization of the material, on the order of nanometers, can be safely neglected, and Raman scattering can be treated as a spatially

* raulcs@fisica.ufmg.br

† ado.jorio@fisica.ufmg.br

incoherent process. There are, however, techniques to improve that resolution, and Tip-Enhanced Raman Spectroscopy (TERS) is one that can reach the nanometers scale [3–6]. In this method, a sharp metallic object is placed close to the measured sample, so close that the strong near field that the tip emits in response to the laser greatly enhances the Raman signal scattered by the sample. As the enhancement only happens in the nanometric region around the tip, one thus obtains both a nanometrically resolved and a greatly enhanced Raman spectroscopic signal.

In the TERS regime, phenomena at the nanometric scale start to play a role in the scattering, in particular if they present spatial coherence. In that case, the symmetry of the excited phonon modes along a wide region of the material can lead to constructive or destructive interferences that affect the TERS signal enhancement in relation to regular far field Raman scattering, in which atoms respond independently from each other. This phenomenon has been experimentally observed in graphene [7, 8] and GaS [9], and a theory has been developed for it assuming that its Raman response in the out-of-plane axis (that is, in the direction perpendicular to the material plane), characterized by the corresponding Raman tensor component, is null [10, 11]. It is known that this component is not null for transition metal dichalcogenides (TMDs) [12], because these materials are not as flat along it as is graphene, so the TERS theory for 2D materials must be extended in order to describe TERS measurements on TMDs [5]. On top of that, one must consider the possibility that the near field of the tip, which has a much stronger spatial gradient than the far field of the excitation laser, might even lead to an out-of-plane response in graphene [13].

In this article, we extend the previous TERS theory for probing 2D materials [10, 11] in three important aspects: (i) the inclusion of the out-of-plane Raman response in the TERS signal, which greatly modifies the contributions to be considered; (ii) we provide the exact analytical solution of the tip-sample-tip (TST), tip-sample (ST) and sample-tip (TS) field propagators, which have previously obtained with an approximation [10, 11], including the out-of-plane contribution; (iii) we show that the TS contribution may be neglected in comparison with the TST and ST terms, when the excitation field is a focused radially polarized Gaussian beam, but only if the out-of-plane sample response is null. In addition, a discussion on the influence of the physical parameters of the model in the TERS intensity signal is made, in a more extensive manner than in previous works, including an analysis of how the medium refractive index leads to an effective tip enhancement factor f_e . We

will argue that, in general, a strong enhancement is needed to distinguish some physical property affecting the behavior of Raman mode intensities in TERS, be it a large f_e , tip radius, relative Raman response or placing the tip very close to the sample. We also use our extended theory to show that graphene TERS experiments seem to strengthen the idea that its out-of-plane Raman response is indeed negligible.

The article is organized as follows. In Sec. II, we introduce the scattering framework used in our TERS theory, while in Sec. III the model for the spatial correlation of the material electric polarizability due to the phonon excitations, which defines the coherence length measured by TERS, is discussed. Section IV presents an interpretation of the TERS scattering as a propagation spatial frequency filter on the polarizability correlation. Section V develops the analytical expression of the propagators of TST, ST and TS components of TERS, and in Sec. VI these are applied to different phonon modes, where the influence of the out-of-plane response is presented. Section VII provides an extensive discussion of our results, with an in-depth analysis of the change in TERS measurements by the physical parameters of the system, given our model, and a comparison with graphene experimental data. We conclude in Sec. VIII.

II. TERS INTENSITY IN A SCATTERING FRAMEWORK

Tip-Enhanced Raman Spectroscopy (TERS) of 2D materials can be modelled by the scattering scheme of Fig. 1. Our treatment will resemble that of Ref. [10], so that we can keep a comparison. A monochromatic electric field $E_i^{(\text{in})}(\mathbf{r}, \omega)$ ($i \in \{x, y, z\}$ is an index for a component of the field) with frequency ω reaches the scattering system composed of the material sample and the tip, and is scattered from there towards a detector far from it. The sample defines the xy plane, and the tip axis, which is perpendicular to the sample plane in our geometry, defines the z axis. In the notation of Fig. 1, z_0 is the closest distance that the tip can be to the sample, when we say that the tip is engaged, z_{tip} is some tip-sample distance larger than z_0 , r_{tip} is the tip radius, and $z = z_{\text{tip}} + r_{\text{tip}}$ defines the distance on the tip axis from the sample to an emitting dipole in the center of the tip, used to model the field scattered by it.

Due to the particular configuration of this two-part system, a series of scattering events can happen. Namely, the field can be scattered by just the sample and go to the detector

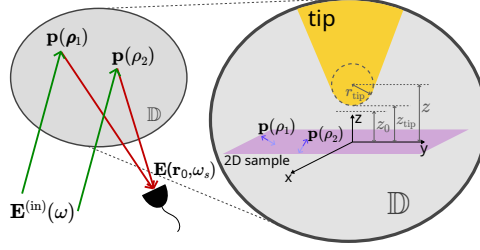


FIG. 1. General scattering framework used in our TERS theory. A monochromatic excitation field $\mathbf{E}^{(\text{in})}(\omega)$, oscillating at frequency ω , reaches a scattering medium with domain \mathbb{D} , and is scattered as the field $\mathbf{E}(\mathbf{r}_0, \omega_s)$ to a detector in \mathbf{r}_0 and at a frequency ω_s . To get the scattered field intensity, we coherently sum the contribution of each pairs of polarizations $\mathbf{p}(\boldsymbol{\rho}_1)$ and $\mathbf{p}(\boldsymbol{\rho}_2)$, excited at points $\boldsymbol{\rho}_1$ and $\boldsymbol{\rho}_2$ in \mathbb{D} . The scattering medium \mathbb{D} contains both the sample and the tip, as well as the optics to collect the scattered field. In the zoom circle, we represent two dipoles $\mathbf{p}(\boldsymbol{\rho}_1)$ and $\mathbf{p}(\boldsymbol{\rho}_2)$ in the sample with non-zero in-plane and out-of-plane components, as a response to the incident and tip electric fields. We define z_{tip} as the distance from the sample plane to the point in the tip closest to the sample, and z_0 as the smallest z_{tip} in a TERS experiment. The tip-sample distance z appearing in the theory localizes the tip emitting dipole inside the tip at a distance r_{tip} from the tip surface, where r_{tip} is the tip radius, so $z = z_{\text{tip}} + r_{\text{tip}}$.

(this term is represented by S); or by just the tip (term T); or be scattered by the tip, then the sample, then go to the detector, which is the tip-sample term (ST in the usual operator notation, right happens first); or first in the sample and then tip, sample-tip term (TS); or it can be a tip-sample-tip event (TST), and so on. This is represented by the series [3]

$$T + S + ST + TS + TST + \dots$$

The T term does not probe the sample, and S is just usual Raman without the tip. The TERS is present in terms ST, TS and TST, and higher-order terms in the series can be neglected for being too weak in the distances that the tip can approach the sample.

A monochromatic field with frequency ω excites the sample at point $\boldsymbol{\rho}$ (we use the greek letter $\boldsymbol{\rho}$ to make it explicit that we are in the 2D plane of the sample), whose i -th component is represented by $E_i(\boldsymbol{\rho}, \omega)$. It may have come from the tip, which is the case for ST and TST terms, or it may have come straight from the source $[E_i^{(\text{in})}(\mathbf{r}, \omega)]$, as in the TS term. It excites an electric polarization $p_j^{(n)}(\boldsymbol{\rho}, \omega_s; \omega)$ at that point $\boldsymbol{\rho}$ with frequency ω_s , in response

to ω , due to some internal (vibrational) mode η , whose response is given by a polarizability tensor $\alpha_{ij}^{(\eta)}$ [14],

$$p_j^{(\eta)}(\boldsymbol{\rho}, \omega_s; \omega) = \sum_i \alpha_{ij}^{(\eta)}(\boldsymbol{\rho}; \omega_s, \omega) E_i(\boldsymbol{\rho}, \omega). \quad (1)$$

This polarization may then create a field propagating straight to the detector (ST), located at point \mathbf{r}_0 , or it may be scattered by the tip before it goes (TS and TST). This creates the field $E_k^{(\eta)}(\mathbf{r}_0, \omega_s)$ at \mathbf{r}_0 with frequency ω_s . We write

$$E_k^{(\eta)}(\mathbf{r}_0, \omega_s) = \frac{\omega_s^2}{\varepsilon_0 c} \sum_j \int_{\mathbb{D}} G_{kj}(\mathbf{r}_0, \boldsymbol{\rho}; \omega_s) p_j^{(\eta)}(\boldsymbol{\rho}, \omega_s; \omega) d^2 \boldsymbol{\rho}, \quad (2)$$

where $G_{kj}(\mathbf{r}_0, \boldsymbol{\rho}; \omega_s)$ is a dyadic Green function containing all the eventual intermediate scatterings between sample and detector.

Since the stationary polarization response can be taken as instantaneous, $p_j^{(\eta)}(\boldsymbol{\rho}, t) = \alpha_{ij}^{(\eta)}(\boldsymbol{\rho}, t) E_i(\boldsymbol{\rho}, t)$, it implies $\alpha_{ij}^{(\eta)}(\boldsymbol{\rho}; \omega_s, \omega) = \alpha_{ij}^{(\eta)}(\boldsymbol{\rho}, \omega - \omega_s)$. Then the scattered field component k due to internal material mode η is

$$E_k^{(\eta)}(\mathbf{r}_0, \omega_s) = \frac{\omega_s^2}{\varepsilon_0 c} \sum_{i,j} \int_{\mathbb{D}} G_{kj}(\mathbf{r}_0, \boldsymbol{\rho}; \omega_s) \times \alpha_{ij}^{(\eta)}(\boldsymbol{\rho}, \omega - \omega_s) E_i(\boldsymbol{\rho}, \omega) d^2 \boldsymbol{\rho}. \quad (3)$$

We can define

$$F_{ijk}(\mathbf{r}; \mathbf{r}_0, \omega_s, \omega) \equiv G_{kj}(\mathbf{r}_0, \boldsymbol{\rho}; \omega_s) E_i(\boldsymbol{\rho}, \omega), \quad (4)$$

such that the detected intensity is $S^{(\eta)}(\mathbf{r}_0, \omega_s) = |\mathbf{E}^{(\eta)}(\mathbf{r}_0, \omega_s)|^2$ at point \mathbf{r}_0 and frequency ω_s is

$$S^{(\eta)}(\mathbf{r}_0, \omega_s) = \frac{\omega_s^4}{\varepsilon_0^2 c^2} \sum_{i,i',j,j',k} \iint_{\mathbb{D}} F_{ijk}^*(\boldsymbol{\rho}_1; \mathbf{r}_0, \omega_s, \omega) F_{i'j'k}(\boldsymbol{\rho}_2; \mathbf{r}_0, \omega_s, \omega) A_{ii',jj'}^{(\eta)}(\boldsymbol{\rho}_2 - \boldsymbol{\rho}_1, \omega - \omega_s) d^2 \boldsymbol{\rho}_1 d^2 \boldsymbol{\rho}_2, \quad (5)$$

where we used

$$A_{ii',jj'}^{(\eta)}(\boldsymbol{\rho}_2 - \boldsymbol{\rho}_1, \omega - \omega_s) \delta(\omega'_s - \omega_s) \equiv \langle \alpha_{ij}^{(\eta)*}(\boldsymbol{\rho}_1, \omega - \omega_s) \alpha_{i'j'}^{(\eta)}(\boldsymbol{\rho}_2, \omega - \omega'_s) \rangle \quad (6)$$

for the two-point correlation function of the electric polarizability of the sampled material. The latter is the crucial physical quantity when we are concerned with spatial coherence, because it carries the response correlation between different points in the sample, telling us which pairs of points respond together to the excitation, and which respond independently

from each other. We will assume, in particular, that the polarizability correlation depends on the absolute difference $|\boldsymbol{\rho}_2 - \boldsymbol{\rho}_1|$, being an isotropic quantity.

By writing the TERS scattered intensity in the form of Eq. (5), making use of the fact that we have at most one sample scattering event, the F functions carry all the propagation information (including the tip-sample geometry from the terms ST, TS and TST) plus the incident electric field, but no phonon information. That is, F contains properties which should be constant across experiments with the same setup but different sampled materials. All the information containing the sample response, like the symmetry of the probed phonon mode, is contained in the correlation function A .

In order to obtain analytical expressions, it will be more convenient to work in the Fourier space with domain $\tilde{\mathbb{D}}$, so we define the pairs

$$\tilde{F}_{ijk}(\mathbf{q}; \mathbf{r}_0, \omega_s, \omega) = \int_{\mathbb{D}} F_{ijk}(\boldsymbol{\rho}; \mathbf{r}_0, \omega_s, \omega) e^{-i\mathbf{q}\cdot\boldsymbol{\rho}} d^2\boldsymbol{\rho}, \quad (7a)$$

$$F_{ijk}(\boldsymbol{\rho}; \mathbf{r}_0, \omega_s, \omega) = \int_{\tilde{\mathbb{D}}} \tilde{F}_{ijk}(\mathbf{q}; \mathbf{r}_0, \omega_s, \omega) e^{-i\mathbf{q}\cdot\boldsymbol{\rho}} \frac{d^2\mathbf{q}}{(2\pi)^2}, \quad (7b)$$

and

$$\begin{aligned} \tilde{A}_{ii',jj'}^{(\eta)}(\mathbf{q}, \omega - \omega_s) &= \int_{\mathbb{D}} A_{ii',jj'}^{(\eta)}(\boldsymbol{\rho}_2 - \boldsymbol{\rho}_1, \omega - \omega_s) \\ &\times e^{-i\mathbf{q}\cdot(\boldsymbol{\rho}_2 - \boldsymbol{\rho}_1)} d^2(\boldsymbol{\rho}_2 - \boldsymbol{\rho}_1), \end{aligned} \quad (8a)$$

$$\begin{aligned} A_{ii',jj'}^{(\eta)}(\boldsymbol{\rho}_2 - \boldsymbol{\rho}_1, \omega - \omega_s) &= \int_{\tilde{\mathbb{D}}} \tilde{A}_{ii',jj'}^{(\eta)}(\mathbf{q}, \omega - \omega_s) \\ &\times e^{i\mathbf{q}\cdot(\boldsymbol{\rho}_2 - \boldsymbol{\rho}_1)} \frac{d^2\mathbf{q}}{(2\pi)^2}. \end{aligned} \quad (8b)$$

The TERS signal of Eq. (5) can then be written as

$$S^{(\eta)}(\mathbf{r}_0, \omega_s) = \frac{\omega_s^4}{\varepsilon_0^2 c^2} \sum_{i,i',j,j',k} \int_{\tilde{\mathbb{D}}} \tilde{F}_{i'j'k}^*(\mathbf{q}; \mathbf{r}_0, \omega_s, \omega) \tilde{F}_{ijk}(\mathbf{q}; \mathbf{r}_0, \omega_s, \omega) \tilde{A}_{ii',jj'}^{(\eta)}(\mathbf{q}, \omega - \omega_s) \frac{d^2\mathbf{q}}{(2\pi)^2}. \quad (9)$$

III. MODEL FOR THE POLARIZABILITY CORRELATION

The model for the polarizability correlation is in the heart of the main extension that we make in the present work in relation to Ref. [10], which is the inclusion of the out-of-plane polarizability response. If we want to model $A_{ii',jj'}^{(\eta)}(\boldsymbol{\rho}_2 - \boldsymbol{\rho}_1, \omega - \omega_s)$, we need the

polarizability $\alpha_{ij}^{(\eta)}(\boldsymbol{\rho}, t)$ due to material vibrations [see Eq. (6)], which is modelled with a first-order expansion of its dependence on the material nuclei positions $Q_k^{(\eta)}(\boldsymbol{\rho}, t)$,

$$\alpha_{ij}^{(\eta)}(\boldsymbol{\rho}, t) = \bar{\alpha}_{ij}^{(\eta)} + \alpha_{ijk}^{(\eta)} \sum_k Q_k^{(\eta)}(\boldsymbol{\rho}, t), \quad (10)$$

where $\alpha_{ijk}^{(\eta)} \equiv (\partial\alpha_{ij}^{(\eta)}/\partial Q_k^{(\eta)})|_{Q_k=0}$ is a third-rank Raman tensor of mode η . We put an η label on Q_k because its dynamics depends on the excited mode. Ignoring the constant part, we get

$$\langle \alpha_{ij}^{(\eta)*}(\boldsymbol{\rho}_1, t_1) \alpha_{i'j'}^{(\eta)}(\boldsymbol{\rho}_2, t_2) \rangle \quad (11)$$

$$= \sum_{k,k'} \tilde{\alpha}_{ijk}^{(\eta)*} \tilde{\alpha}_{i'j'k'}^{(\eta)} \langle Q_k^{(\eta)}(\boldsymbol{\rho}_1, t_1) Q_{k'}^{(\eta)}(\boldsymbol{\rho}_2, t_2) \rangle, \quad (12)$$

which can be very cumbersome to calculate from first principles, and we would need to know the exact dynamics of the driven phonons if we were to do it.

Instead, we adopt the phenomenological approach of Ref. [10] and write, in the frequency domain,

$$A_{ii',jj'}^{(\eta)}(\boldsymbol{\rho}_2 - \boldsymbol{\rho}_1, \omega - \omega_s) \quad (13)$$

$$= \alpha_{ij}^{(\eta)*} \alpha_{i'j'}^{(\eta)} \Omega^{(\eta)}(\omega - \omega_s) \mathcal{L}^{(\eta)}(|\boldsymbol{\rho}_2 - \boldsymbol{\rho}_1|; L_c), \quad (14)$$

where the $\alpha_{ij}^{(\eta)}$ are the Raman tensors of mode η that carry the tensorial part of the polarizability correlation, $\Omega^{(\eta)}(\omega - \omega_s)$ determines the phonon spectrum of mode η , and $\mathcal{L}^{(\eta)}(|\boldsymbol{\rho}_2 - \boldsymbol{\rho}_1|; L_c)$ is the spatial part, characterized by a single length parameter L_c . The meaning of L_c is the $|\boldsymbol{\rho}_2 - \boldsymbol{\rho}_1|$ distance over which \mathcal{L} is above a certain value, so it plays the part of the coherence length of the phononic polarization induced in the material, and we call it the TERS coherence length. As $L_c \rightarrow 0$, we expect that $\mathcal{L} \rightarrow \delta^{(2)}(|\boldsymbol{\rho}_2 - \boldsymbol{\rho}_1|)$, and as $L_c \rightarrow \infty$, we expect that $\mathcal{L} \rightarrow C$, C being a constant. This is what we expect for a correlation function, because only such a limit can provide the totally uncorrelated scattering [10] when plugging $\mathcal{L} \rightarrow \delta^{(2)}(|\boldsymbol{\rho}_2 - \boldsymbol{\rho}_1|)$ into Eq. (5).

A reasonable choice for a phenomenological \mathcal{L} fulfilling these properties is a Gaussian function with unit integral [10],

$$\mathcal{L}^{(\eta)}(|\boldsymbol{\rho}_2 - \boldsymbol{\rho}_1|; L_c) = \frac{1}{\pi L_c^2} e^{-|\boldsymbol{\rho}_2 - \boldsymbol{\rho}_1|^2/L_c^2}, \quad (15a)$$

$$\tilde{\mathcal{L}}^{(\eta)}(\mathbf{q}; L_c) = e^{-|\mathbf{q}|^2 L_c^2/4}. \quad (15b)$$

This choice has the particular important property that its norm, equal to $1/(2\pi L_c^2)$, decreases as L_c increases. In Sec. IV we will see that the TERS signal can be interpreted as the internal product between a function $\mathcal{J}^{(n)}$. Then, for a fixed $\mathcal{J}^{(n)}$, which means all experimental parameters being fixed, as L_c gets larger its internal product with $\mathcal{L}^{(n)}$ can only get smaller, because of the decreasing norm of the latter. This implies that the TERS intensity decreases as L_c increases if we use Eq. (13) and Eq. (15) as the model for the polarizability correlation.

Phonons of modes A_1 and E_{2g} can yield a strong Raman signal in both graphene and TMDs [15], and can also show a significant enhancement in TERS [7, 16]. Mode A_1 is viewed as a scalar mode in graphene [17], but it comes from an out-of-plane oscillation in TMDs [18]. From symmetry considerations, their Raman polarizability tensors can be written in the general forms

$$\alpha_{ij}^{(A_1)} = \bar{\alpha}^{(A_1)} \begin{bmatrix} 1 & 0 & 0 \\ 0 & 1 & 0 \\ 0 & 0 & \nu \end{bmatrix}_{ij}, \quad (16a)$$

$$\alpha_{ij}^{(E_{2g,x})} = \bar{\alpha}^{(E_{2g})} \begin{bmatrix} 0 & 1 & 0 \\ 1 & 0 & 0 \\ 0 & 0 & 0 \end{bmatrix}_{ij}, \quad (16b)$$

$$\alpha_{ij}^{(E_{2g,y})} = \bar{\alpha}^{(E_{2g})} \begin{bmatrix} 1 & 0 & 0 \\ 0 & -1 & 0 \\ 0 & 0 & 0 \end{bmatrix}_{ij}. \quad (16c)$$

In comparison with Ref. [10], we included the possibility of a non-zero z component of the polarizability in the A_1 Raman tensor as the ν parameter, which will demand the calculation of new terms in the TERS signal. It was known that differences in the symmetry between the two modes lead to a different decay in the TERS signal between them, when varying the tip-sample distance z [7, 8, 10], and $\nu > 0$ will be yet another factor to influence these differences, which we will investigate.

For TMDs, $\nu > 0$ must certainly be included in the treatment, with a striking experimental value of 4 being found in the literature [12]. In graphene, in regular Raman without the tip, the excitation field can be taken as constant in a region of the order of its wavelength, and due to a z -axis symmetry of the charge distribution in the material, the z contribution

to the polarization excited by this constant field cancels out, yielding $\nu = 0$. However, in the presence of the near field emitted by the tip, which varies on a nanometer scale, this symmetry can be broken, because the charge displaced in the material at $z > 0$ will be considerably different than that at $z < 0$ [13]. This opens the possibility for $\nu > 0$ to be considered in graphene in a TERS setting, and we aim to investigate how this parameter may influence graphene TERS measurements.

IV. PROPAGATION AS A SPATIAL FREQUENCY FILTER ON THE CORRELATION

It is convenient to define a quantity $\mathcal{I}^{(\eta)}$ that contains the propagation and tensorial parts of the TERS signal of mode η by

$$\tilde{\mathcal{I}}^{(\eta)}(\mathbf{q}; \mathbf{r}_0, \omega_s, \omega) \equiv \sum_k \left(\sum_{i', j'} \tilde{F}_{i'j'k}^*(\mathbf{q}; \mathbf{r}_0, \omega_s, \omega) \alpha_{i'j'}^{(\eta)*} \right) \left(\sum_{i, j} \tilde{F}_{ijk}(\mathbf{q}; \mathbf{r}_0, \omega_s, \omega) \alpha_{ij}^{(\eta)} \right). \quad (17)$$

Then, with Eq. (9) and (13), the TERS intensity is written as

$$S^{(\eta)}(\mathbf{r}_0, \omega_s) = \frac{\omega_s^4}{\varepsilon_0^2 c^2} \Omega^{(\eta)}(\omega - \omega_s) \int_{\mathbb{D}} \tilde{\mathcal{I}}^{(\eta)}(\mathbf{q}; \mathbf{r}_0, \omega_s, \omega) \tilde{\mathcal{L}}^{(\eta)}(\mathbf{q}; L_c) \frac{d^2 \mathbf{q}}{(2\pi)^2}, \quad (18)$$

with the dependence on the coherence length L_c being isolated in $\tilde{\mathcal{L}}^{(\eta)}$. This has the nice interpretation that the propagation-tensorial function $\tilde{\mathcal{I}}^{(\eta)}(\mathbf{q}; z)$ acts like a spatial frequency filter over the correlation $\tilde{\mathcal{L}}^{(\eta)}(\mathbf{q}; L_c)$, which is then integrated over all wave vectors \mathbf{q} . In other words, the TERS intensity signal is proportional to the internal product between propagation (which depends on z) and the polarizability correlation.

Taking one step further, we can use the fact that the isotropic $\mathcal{L}^{(\eta)}$ is a function of the modulus $|\mathbf{q}| \equiv q$, but not its angle φ_q , and defining $\tilde{\mathcal{J}}^{(\eta)}(q; \mathbf{r}_0, \omega_s, \omega) \equiv \int_0^{2\pi} \tilde{\mathcal{I}}^{(\eta)}(\mathbf{q}; \mathbf{r}_0, \omega_s, \omega) d\varphi_q$ yields

$$S^{(\eta)}(\mathbf{r}_0, \omega_s) = \frac{\omega_s^4}{\varepsilon_0^2 c^2} \frac{\Omega^{(\eta)}(\omega - \omega_s)}{(2\pi)^2} \int_0^\infty \tilde{\mathcal{J}}^{(\eta)}(q; z, \mathbf{r}_0, \omega_s, \omega) \tilde{\mathcal{L}}^{(\eta)}(q; L_c) q dq, \quad (19)$$

where we explicitly state that $\tilde{\mathcal{J}}^{(\eta)}$ depends on the tip-sample distance z . Then, from Parseval's theorem on cylindrically symmetric functions [19], the internal product can be taken with respect to the spatial variable $\rho \equiv |\boldsymbol{\rho}_2 - \boldsymbol{\rho}_1|$,

$$S^{(\eta)}(\mathbf{r}_0, \omega_s) = \frac{\omega_s^4}{\varepsilon_0^2 c^2} \frac{\Omega^{(\eta)}(\omega - \omega_s)}{(2\pi)^2} \int_0^\infty \mathcal{J}^{(\eta)}(\rho; z, \mathbf{r}_0, \omega_s, \omega) \mathcal{L}^{(\eta)}(\rho; L_c) \rho d\rho, \quad (20)$$

where $\mathcal{J}^{(n)}(\rho; z, \mathbf{r}_0, \omega_s, \omega)$ is the zeroth-order inverse Hankel transform of $\tilde{\mathcal{J}}^{(n)}(q; z, \mathbf{r}_0, \omega_s, \omega)$,

$$\mathcal{J}^{(n)}(\rho; z, \mathbf{r}_0, \omega_s, \omega) \equiv 2\pi \int_0^\infty \tilde{\mathcal{J}}^{(n)}(q; z, \mathbf{r}_0, \omega_s, \omega) J_0(\rho q) q dq, \quad (21)$$

and analogously for $\mathcal{L}^{(n)}(\rho; L_c)$, whose expression is that in Eq. (15) for $\rho = |\boldsymbol{\rho}_2 - \boldsymbol{\rho}_1|$.

V. FIELD PROPAGATION

In this section, we calculate the TST, ST, and TS contributions to the propagation functions F , defined in Eq. (4). As noted, these functions carry all the geometrical properties of the sample+tip setup and the incident field, but do not include the phonon polarizability response of the medium, which we treated in the previous section. The respective propagators for the TST, ST, and TS terms are [10]

$$F_{ijk}^{\text{TST}}(\boldsymbol{\rho}; \mathbf{r}_0, \omega_s, \omega) = \left[\sum_{n,n'} G_{kn'}^{\text{FF}}(\mathbf{r}_0, z\hat{\mathbf{z}}; \omega_s) \frac{\omega_s^2}{\varepsilon_0 c^2} \alpha_{nn'}^{\text{tip}} G_{nj}^{\text{NF}}(z\hat{\mathbf{z}}, \boldsymbol{\rho}; \omega_s) \right] \times \left[\sum_{l,l'} G_{il'}^{\text{NF}}(\boldsymbol{\rho}, z\hat{\mathbf{z}}; \omega) \frac{\omega^2}{\varepsilon_0 c^2} \alpha_{ll'}^{\text{tip}} E_l(z\hat{\mathbf{z}}, \omega) \right], \quad (22a)$$

$$F_{ijk}^{\text{ST}}(\boldsymbol{\rho}; \mathbf{r}_0, \omega_s, \omega) = G_{kj}^{\text{FF}}(\mathbf{r}_0, \boldsymbol{\rho}; \omega_s) \left[\sum_{l,l'} G_{il'}^{\text{NF}}(\boldsymbol{\rho}, z\hat{\mathbf{z}}; \omega) \frac{\omega^2}{\varepsilon_0 c^2} \alpha_{ll'}^{\text{tip}} E_l(z\hat{\mathbf{z}}, \omega) \right], \quad (22b)$$

$$F_{ijk}^{\text{TS}}(\boldsymbol{\rho}; \mathbf{r}_0, \omega_s, \omega) = \left[\sum_{n,n'} G_{kn'}^{\text{FF}}(\mathbf{r}_0, z\hat{\mathbf{z}}; \omega_s) \frac{\omega_s^2}{\varepsilon_0 c^2} \alpha_{nn'}^{\text{tip}} G_{nj}^{\text{NF}}(z\hat{\mathbf{z}}, \boldsymbol{\rho}; \omega_s) \right] E_i(\boldsymbol{\rho}, \omega), \quad (22c)$$

where $G_{il'}^{\text{NF}}(\boldsymbol{\rho}, z\hat{\mathbf{z}}; \omega)$ is a near field propagator from $z\hat{\mathbf{z}}$ (on tip axis) to $\boldsymbol{\rho}$ (on sample plane), from polarization i to l' , at frequency ω , and analogously for the other G functions, with FF for a far field propagator. Also note that we assumed that the tip response $\alpha_{nn'}^{\text{tip}}$ is the same for ω and ω_s . With this notation, regular Raman without the tip is

$$F_{ijk}^{\text{S}}(\boldsymbol{\rho}; \mathbf{r}_0, \omega_s, \omega) = G_{kj}^{\text{FF}}(\mathbf{r}_0, \boldsymbol{\rho}; \omega_s) E_i(\boldsymbol{\rho}, \omega). \quad (23)$$

We will assume that the tip responds much more strongly in the z direction than on the sample plane directions and is the same for ω and ω_s , that is, $\alpha_{nn'}^{\text{tip}}(\omega) \approx 2\pi\varepsilon_0 r_{\text{tip}}^3 f_e \delta_{nz} \delta_{n'z}$, where r_{tip} is the tip radius and f_e is a real enhancement factor. This approximation was used in Ref. [10, 11] and it is equivalent to the assumption that the tip emits radiation as a point dipole, which has been experimentally verified as a valid approximation in Ref. [20].

Then, up to a phase factor, the near field propagator in a medium with refractive index n is [3]

$$G_{ij}^{\text{NF}}(\boldsymbol{\rho}, z\hat{\mathbf{z}}; \omega) = \frac{c^2}{4\pi n^2 \omega^2} \left[-\delta_{ij} \frac{1}{(\rho^2 + z^2)^{3/2}} + \frac{3r_i r_j}{(\rho^2 + z^2)^{5/2}} \right], \quad (24)$$

where δ_{ij} is the Kronecker delta, $\mathbf{r} \equiv \boldsymbol{\rho} + z\hat{\mathbf{z}}$, with $\boldsymbol{\rho} \equiv x\hat{\mathbf{x}} + y\hat{\mathbf{y}}$, such that $r_x \equiv x$, $r_y \equiv y$ and $r_z \equiv z$, and $\rho \equiv |\boldsymbol{\rho}|$. Note that interchanging either i and j or $\boldsymbol{\rho}$ and $z\hat{\mathbf{z}}$ does not change the expression. In comparison to Ref. [10, 11], we have to include the z response of the sample, because we are open to $\nu > 0$ in Eq. (16).

To take advantage of the cylindrical symmetry of the system, we will use adimensional polar coordinates in the plane, $\varrho \equiv \rho/z$, and φ_ϱ defined by $r_i/z \equiv [\delta_{iz} + (1 - \delta_{iz})\varrho]\psi_i(\varphi_\varrho)$, where $\psi_x(\varphi_\varrho) \equiv \cos(\varphi_\varrho)$, $\psi_y(\varphi_\varrho) \equiv \sin(\varphi_\varrho)$ and $\psi_z(\varphi_\varrho) \equiv 1$. In this notation, which will be used in all of Sec. V, while δ_{iz} survives for $i = z$, $(1 - \delta_{iz})$ identifies the term that survives when $i \neq z$. Then, we can write

$$G_{ij}^{\text{NF}}(\varrho, \varphi_\varrho, z; \omega) = \frac{c^2}{4\pi n^2 \omega^2} \left(\frac{1}{z^3} \right) \left\{ -\delta_{ij} \frac{1}{(\varrho^2 + 1)^{3/2}} + 3[\delta_{iz} + (1 - \delta_{iz})\varrho][\delta_{jz} + (1 - \delta_{jz})\varrho] \frac{\psi_i(\varphi_\varrho)\psi_j(\varphi_\varrho)}{(\varrho^2 + 1)^{5/2}} \right\}, \quad (25)$$

which seems cumbersome, but will allow us to solve some integrals.

In our treatment, we will use the assumption that the radial component of the incident electric field in the sample+tip system can be neglected, because the use of a focused radially polarized Gaussian beam yields a z component much stronger than the radial one (see Appendix A). This causes the TS in-plane component contribution to be negligible in comparison with TST and ST, so it is safe to assume it null. In the case that TS out-of-plane is small, thus being comparable to TS in-plane, the error in including one and not the other will not be significant, because both will be negligible in comparison with TST and ST. It is worth noting that in Ref. [11] the authors assume that the radially polarized field at the vicinity of the tip has an intensity of about 1/3 of that of the z component, which would imply that the radially polarized TS component cannot be neglected. In Appendix A we assume a strong focus specified by an objective numerical aperture (NA) of 1.4, leading to the negligible radial component, as seen in Fig. 7. For weaker focusing, for instance $\text{NA} \lesssim 1$, the radial TS contribution might still be important.

In addition, since the z component of the incident field does not vary significantly in the region around the tip, we will neglect its dependence on \mathbf{r} and z . We also take advantage of the cylindrical symmetry of the problem and write the far field propagator as the sum of an axial g_z^{FF} and a radial $g_{\parallel}^{\text{FF}}$ part,

$$G_{kj}^{\text{FF}} = \delta_{kj}[g_z^{\text{FF}}\delta_{jz} + g_{\parallel}^{\text{FF}}(1 - \delta_{jz})]. \quad (26)$$

These factors indicate how much light with each polarization is collected from the scattering and directed towards the detectors. If g_z^{FF} and $g_{\parallel}^{\text{FF}}$ differ, it means that the system collects one polarization better than the other, and this will depend on the particular geometry of the experimental setup.

A. Tip-sample-tip (TST) term

We take the spatial Fourier transform of Eq. (22a),

$$F_{ijk}^{\text{TST}}(\mathbf{q}; \mathbf{r}_0, \omega_s, \omega) = \frac{\omega^2 \omega_s^2}{\varepsilon_0^2 c^4} (\alpha_{zz}^{\text{tip}})^2 G_{kz}^{\text{FF}}(\mathbf{r}_0, \mathbf{0}; \omega_s) E_z(\omega) \quad (27)$$

$$\times \int_{\mathbb{D}} G_{zj}^{\text{NF}}(z\hat{\mathbf{z}}, \boldsymbol{\rho}; \omega_s) G_{iz}^{\text{NF}}(\boldsymbol{\rho}, z\hat{\mathbf{z}}; \omega) e^{-i\mathbf{q}\cdot\boldsymbol{\rho}} d^2\boldsymbol{\rho}, \quad (28)$$

where the far field does not vary much so we can take it as coming from the origin $\mathbf{0}$. We define the adimensional cylindrical coordinates in the wave vector space as $\xi \equiv |\mathbf{q}|z$, and φ_ξ defined by $q_{iz} \equiv \xi\psi_i(\varphi_\xi)$, with $i \in \{x, y\}$. Plugging the propagators from Eq. (25),

$$F_{ijk}^{\text{TST}}(\mathbf{q}; \mathbf{r}_0, \omega_s, \omega) = \left(\frac{\alpha_{zz}^{\text{tip}}}{4\pi\varepsilon}\right)^2 \delta_{kz} g_z^{\text{FF}} E_z(\omega) \left(\frac{\pi}{z^4}\right) h_{ij}(\xi, \varphi_\xi), \quad (29)$$

where we used $\varepsilon \equiv n^2\varepsilon_0$, and defined

$$h_{ij}(\xi, \varphi_\xi) \equiv \frac{1}{\pi} \int_0^\infty \int_0^{2\pi} \left\{ \begin{aligned} & 9 [\delta_{iz} + (1 - \delta_{iz})\varrho][\delta_{jz} + (1 - \delta_{jz})\varrho] \frac{\psi_i(\varphi_\varrho)\psi_j(\varphi_\varrho)}{(\varrho^2 + 1)^5} + \delta_{iz}\delta_{jz} \frac{1}{(\varrho^2 + 1)^3} \\ & - 3\delta_{iz}[\delta_{jz} + (1 - \delta_{jz})\varrho] \frac{\psi_j(\varphi_\varrho)}{(\varrho^2 + 1)^4} - 3[\delta_{iz} + (1 - \delta_{iz})\varrho]\delta_{jz} \frac{\psi_i(\varphi_\varrho)}{(\varrho^2 + 1)^4} \end{aligned} \right\} \\ \times e^{-i\xi\rho \cos(\varphi_\xi - \varphi_\rho)} \varrho d\varrho d\varphi_\varrho. \quad (30)$$

We can write this expression in a more insightful manner, to make it easier to identify the contributions of each components,

$$\begin{aligned}
h_{ij}(\xi, \varphi_\xi) = \frac{1}{\pi} \int_0^\infty \int_0^{2\pi} \left\{ \delta_{iz} \delta_{jz} \left[9 \frac{1}{(\varrho^2 + 1)^5} + \frac{1}{(\varrho^2 + 1)^3} - 6 \frac{1}{(\varrho^2 + 1)^4} \right] \right. \\
+ [(1 - \delta_{iz})\delta_{jz}\psi_i(\varphi_\varrho) + \delta_{iz}(1 - \delta_{jz})\psi_j(\varphi_\varrho)] \left[9 \frac{\varrho}{(\varrho^2 + 1)^5} - 3 \frac{\varrho}{(\varrho^2 + 1)^4} \right] \\
\left. + 9(1 - \delta_{iz})(1 - \delta_{jz})\psi_i(\varphi_\varrho)\psi_j(\varphi_\varrho) \frac{\rho^2}{(\varrho^2 + 1)^5} \right\} e^{-i\xi\rho \cos(\phi_\xi - \phi_\rho)} \varrho d\varrho d\phi_\varrho.
\end{aligned} \tag{31}$$

The top term between the curly brackets in Eq. (31) is the one for $i = j = z$, the middle one for $i \in \{x, y\}$ and $j = z$ and vice-versa, and the bottom one for $i, j \in \{x, y\}$. If we set $i, j \in \{x, y\}$, we get back to Ref. [10, 11], where the sample does not respond in direction z .

To solve these integrals analytically, we use the Jacobi-Anger expansion [21],

$$e^{-i\xi\varrho \cos(\varphi_\xi - \varphi_\varrho)} = J_0(\xi\varrho) + 2 \sum_{n=1}^{\infty} (-i)^n J_n(\xi\varrho) \cos(n\varphi_\xi - n\varphi_\varrho), \tag{32}$$

so that we can solve the angular integral separately from the radial one. For that matter, we must use trigonometric identities and orthogonality relations for trigonometric functions (see Appendix B), arriving at

$$\begin{aligned}
h_{ij}(\xi, \varphi_\xi) = \int_0^\infty \left\{ \delta_{iz} \delta_{jz} [2J_0(\xi\varrho)] \left[9 \frac{1}{(\varrho^2 + 1)^5} + \frac{1}{(\varrho^2 + 1)^3} - 6 \frac{1}{(\varrho^2 + 1)^4} \right] \right. \\
+ [(1 - \delta_{iz})\delta_{jz}\psi_i(\varphi_\xi) + \delta_{iz}(1 - \delta_{jz})\psi_j(\varphi_\xi)] [-2i] \left[9 \frac{\varrho}{(\varrho^2 + 1)^5} - 3 \frac{\varrho}{(\varrho^2 + 1)^4} \right] \\
\left. + 9(1 - \delta_{iz})(1 - \delta_{jz}) [\delta_{ij}J_0(\xi\varrho) - \tau_{ij}(\varphi_\xi)J_2(\xi\varrho)] \frac{\rho^2}{(\varrho^2 + 1)^5} \right\} \varrho d\varrho,
\end{aligned} \tag{33}$$

where

$$\tau_{ij}(\phi_\xi) \equiv \begin{bmatrix} \cos(2\phi_\xi) & \sin(2\phi_\xi) \\ \sin(2\phi_\xi) & -\cos(2\phi_\xi) \end{bmatrix}_{ij}. \tag{34}$$

In Appendix C, we show how the solutions of these integrals come from the theory of Hankel (or Bessel) transforms [19, 22, 23]. With that we can write an exact analytical

expression for $h_{ij}(\xi, \varphi_\xi)$,

$$\begin{aligned}
h_{ij}(\xi, \varphi_\xi) = & 2 \delta_{iz} \delta_{jz} \left[\frac{9}{384} \xi^4 K_4(\xi) - \frac{6}{48} \xi^3 K_3(\xi) + \frac{1}{8} \xi^2 K_2(\xi) \right] \\
& - 2i [(1 - \delta_{iz}) \delta_{jz} \psi_i(\varphi_\xi) + \delta_{iz} (1 - \delta_{jz}) \psi_j(\varphi_\xi)] \left[\frac{9}{384} \xi^4 K_3(\xi) - \frac{3}{48} \xi^3 K_2(\xi) \right] \\
& + (1 - \delta_{iz})(1 - \delta_{jz}) \left[\delta_{ij} \frac{9}{384} (2\xi^3 K_3(\xi) - \xi^4 K_2(\xi)) - \tau_{ij}(\varphi_\xi) \frac{9}{384} \xi^4 K_2(\xi) \right],
\end{aligned} \tag{35}$$

where $K_\nu(\xi)$ is the modified Bessel function of the second kind of order ν .

B. Tip-sample (ST) term

To write the ST term, we take the spatial Fourier transform of Eq. (22b),

$$F_{ijk}^{\text{ST}}(\mathbf{q}; \mathbf{r}_0, \omega_s, \omega) = \frac{\omega^2}{\varepsilon_0 c^2} \alpha_{zz}^{\text{tip}} G_{kj}^{\text{FF}}(\mathbf{r}_0, \mathbf{0}; \omega_s) E_z(\omega) \int_{\mathbb{D}} G_{iz}^{\text{NF}}(\boldsymbol{\rho}, z\hat{\mathbf{z}}; \omega) e^{-i\mathbf{q}\cdot\boldsymbol{\rho}} d^2\boldsymbol{\rho}, \tag{36}$$

where again we assume the far field as coming from the origin $\mathbf{0}$. Plugging the propagator from Eq. (25),

$$F_{ijk}^{\text{ST}}(\mathbf{q}; \mathbf{r}_0, \omega_s, \omega) = \left(\frac{\alpha_{zz}^{\text{tip}}}{4\pi\varepsilon} \right) \delta_{kj} [g_z^{\text{FF}} \delta_{jz} + g_{\parallel}^{\text{FF}} (1 - \delta_{jz})] E_z(\omega) \left(\frac{\pi}{z} \right) a_i(\xi, \varphi_\xi), \tag{37}$$

where we defined

$$\begin{aligned}
a_i(\xi, \varphi_\xi) \equiv & \frac{1}{\pi} \int_0^\infty \int_0^{2\pi} \left\{ \delta_{iz} \left[3 \frac{1}{(\varrho^2 + 1)^{5/2}} - \frac{1}{(\varrho^2 + 1)^{3/2}} \right] \right. \\
& \left. + 3(1 - \delta_{iz}) \psi_i(\varphi_\varrho) \frac{\varrho}{(\varrho^2 + 1)^{5/2}} \right\} e^{-i\xi\rho \cos(\varphi_\xi - \varphi_\varrho)} \varrho d\varrho d\varphi_\varrho.
\end{aligned} \tag{38}$$

In Eq. (38), if we set $i \in \{x, y\}$, only the last term between the curly brackets survives and we get back to Ref. [10, 11], where the sample z component does not respond.

Using the results from Appendix B, the angular integrals can be solved analytically,

$$\begin{aligned}
a_i(\xi, \varphi_\xi) = & \int_0^\infty \left\{ \delta_{iz} [2J_0(\xi\varrho)] \left[3 \frac{1}{(\varrho^2 + 1)^{5/2}} - \frac{1}{(\varrho^2 + 1)^{3/2}} \right] \right. \\
& \left. - 6i(1 - \delta_{iz}) \psi_i(\varphi_\xi) J_1(\xi\varrho) \frac{\varrho}{(\varrho^2 + 1)^{5/2}} \right\} \varrho d\varrho d\varphi_\varrho.
\end{aligned} \tag{39}$$

The results from Appendix C then provide the exact analytical expression for $a_i(\xi, \varphi_\xi)$,

$$a_i(\xi, \varphi_\xi) = 2 [\delta_{iz} - i(1 - \delta_{iz}) \psi_i(\varphi_\xi)] \xi e^{-\xi}. \tag{40}$$

C. Sample-tip (TS) term

Taking the Fourier transform of Eq. (22c),

$$F_{ijk}^{\text{TS}}(\boldsymbol{\rho}; \mathbf{r}_0, \omega_s, \omega) = \frac{\omega_s^2}{\varepsilon_0 c^2} \alpha_{zz}^{\text{tip}} G_{kz}^{\text{FF}}(\mathbf{r}_0, \mathbf{0}; \omega_s) \int_{\mathbb{D}} G_{zj}^{\text{NF}}(z\hat{\mathbf{z}}, \boldsymbol{\rho}; \omega_s) E_i(\boldsymbol{\rho}, \omega) e^{-i\mathbf{q}\cdot\boldsymbol{\rho}} d^2\boldsymbol{\rho}, \quad (41)$$

we see, distinctly from the TST and ST terms, that the Field may vary with $\boldsymbol{\rho}$, because here it reaches the sample first. However, we know that the xy -plane field components are very weak in the vicinity of the tip, where the near field propagator contributes with relevant magnitude, so we will work only with the z component, which we may consider as constant over a 50 nm radius around the tip (see Appendix A). At this distance the near field contribution certainly vanishes, so only atoms very close to the tip will contribute to TS. Then, plugging the propagator from Eq. (25),

$$F_{ijk}^{\text{TS}}(\mathbf{q}; \mathbf{r}_0, \omega_s, \omega) = \left(\frac{\alpha_{zz}^{\text{tip}}}{4\pi\varepsilon} \right) \delta_{kz} g_z^{\text{FF}} \delta_{iz} E_z(\omega) \left(\frac{\pi}{z} \right) a_j(\xi, \varphi_\xi), \quad (42)$$

with $a_j(\xi, \varphi_\xi)$ defined in Eq. (38) and evaluated to Eq. (40).

D. Sum of all contributions

The full propagator is the sum of all the contributions that we have calculated,

$$F_{ijk}(\mathbf{q}; \mathbf{r}_0, \omega_s, \omega) = F_{ijk}^{\text{TST}}(\mathbf{q}; \mathbf{r}_0, \omega_s, \omega) + F_{ijk}^{\text{ST}}(\mathbf{q}; \mathbf{r}_0, \omega_s, \omega) + F_{ijk}^{\text{TS}}(\mathbf{q}; \mathbf{r}_0, \omega_s, \omega), \quad (43)$$

whose explicit form reads

$$\begin{aligned} F_{ijk}(\mathbf{q}; \mathbf{r}_0, \omega_s, \omega) &= \delta_{kz} g_z^{\text{FF}} E_z(\omega) \\ &\times \left\{ \left(\frac{\alpha_{zz}^{\text{tip}}}{4\pi\varepsilon} \right)^2 \frac{\pi}{z^4} h_{ij}(\xi, \varphi_\xi) + \left(\frac{\alpha_{zz}^{\text{tip}}}{4\pi\varepsilon} \right) \frac{\pi}{z} [\delta_{jz} a_i(\xi, \varphi_\xi) + a_j(\xi, \varphi_\xi) \delta_{iz}] \right\} \\ &+ (1 - \delta_{kz}) g_{\parallel}^{\text{FF}} E_z(\omega) \left(\frac{\alpha_{zz}^{\text{tip}}}{4\pi\varepsilon} \right) \frac{\pi}{z} \delta_{kj} a_i(\xi, \varphi_\xi). \end{aligned} \quad (44)$$

The index associated with the detected field polarization is k , so if we group the components by this index, we can see which contributions interfere with each other. Namely, TST and TS contain only a $k = z$ contribution (because they scatter from the tip last), while ST contributes with all components, $k \in \{x, y, z\}$ (because it scatters from the sample last). This means that interference between contributions TST, ST and TS will appear in

the scattered z component, because they are scattered towards the detector in the same polarization,

$$F_{ijz} = F_{ijz}^{\text{TST}} + F_{ijz}^{\text{ST}} + F_{ijz}^{\text{TS}}, \quad (45a)$$

$$F_{ijx} = F_{ijx}^{\text{ST}}, \quad (45b)$$

$$F_{ijy} = F_{ijy}^{\text{ST}}. \quad (45c)$$

Note that in Ref. [10], in which there is no TS contribution and no sample z response, the total contribution is just a sum of TST and ST intensities, without any interference, because there $F_{ijz} = F_{ijz}^{\text{TST}}$.

VI. TERS SIGNAL OF PARTICULAR PHONON MODES

In the previous section, the propagation of the electromagnetic field in the TERS signal was studied independently from the sample properties. The phonon symmetries, however, given for instance in the Raman tensors $\alpha^{(\eta)}$ of Eq. (16), select the polarization of the scattered light, so not all components of the tensor F_{ijk} participate in the TERS signal of a given mode. To understand which i, j components of the tensor F_{ijk} are probed by each mode, and in which combination, we check its multiplication with the $\alpha^{(\eta)}$ for each mode,

$$\sum_{i,j} F_{ijk} \alpha_{ij}^{(A_1)} = \bar{\alpha}^{(A_1)} (F_{xxk} + F_{yyk} + \nu F_{zzk}), \quad (46a)$$

$$\sum_{i,j} F_{ijk} \alpha_{ij}^{(E_{2g},x)} = \bar{\alpha}^{(E_{2g})} (F_{xyk} + F_{yxk}), \quad (46b)$$

$$\sum_{i,j} F_{ijk} \alpha_{ij}^{(E_{2g},y)} = \bar{\alpha}^{(E_{2g})} (F_{xxk} - F_{yyk}). \quad (46c)$$

Explicitly, using Eq. (44),

$$\begin{aligned} \sum_{i,j} F_{ijk} \alpha_{ij}^{(A_1)} = \bar{\alpha}^{(A_1)} E_z(\omega) \left\{ \right. & \delta_{kz} g_z^{\text{FF}} \left(\frac{\alpha_{zz}^{\text{tip}}}{4\pi\epsilon} \right)^2 \frac{\pi}{z^4} [h_{xx}(\xi, \varphi_\xi) + h_{yy}(\xi, \varphi_\xi)] \\ & + g_{\parallel}^{\text{FF}} \left(\frac{\alpha_{zz}^{\text{tip}}}{4\pi\epsilon} \right) \frac{\pi}{z} [\delta_{kx} a_x(\xi, \varphi_\xi) + \delta_{ky} a_y(\xi, \varphi_\xi)] \\ & \left. + \nu \delta_{kz} g_z^{\text{FF}} \left[\left(\frac{\alpha_{zz}^{\text{tip}}}{4\pi\epsilon} \right)^2 \frac{\pi}{z^4} h_{zz}(\xi, \varphi_\xi) + 2 \left(\frac{\alpha_{zz}^{\text{tip}}}{4\pi\epsilon} \right) \frac{\pi}{z} a_z(\xi, \varphi_\xi) \right] \right\}, \end{aligned} \quad (47a)$$

$$\sum_{i,j} F_{ijk} \alpha_{ij}^{(E_{2g},x)} = \bar{\alpha}^{(E_{2g})} E_z(\omega) \left\{ \delta_{kz} g_z^{\text{FF}} \left(\frac{\alpha_{zz}^{\text{tip}}}{4\pi\varepsilon} \right)^2 \frac{\pi}{z^4} [h_{xy}(\xi, \varphi_\xi) + h_{yx}(\xi, \varphi_\xi)] \right. \\ \left. + g_{\parallel}^{\text{FF}} \left(\frac{\alpha_{zz}^{\text{tip}}}{4\pi\varepsilon} \right) \frac{\pi}{z} [\delta_{kx} a_y(\xi, \varphi_\xi) + \delta_{ky} a_x(\xi, \varphi_\xi)] \right\}, \quad (47b)$$

$$\sum_{i,j} F_{ijk} \alpha_{ij}^{(E_{2g},y)} = \bar{\alpha}^{(E_{2g})} E_z(\omega) \left\{ \delta_{kz} g_z^{\text{FF}} \left(\frac{\alpha_{zz}^{\text{tip}}}{4\pi\varepsilon} \right)^2 \frac{\pi}{z^4} [h_{xx}(\xi, \varphi_\xi) - h_{yy}(\xi, \varphi_\xi)] \right. \\ \left. + g_{\parallel}^{\text{FF}} \left(\frac{\alpha_{zz}^{\text{tip}}}{4\pi\varepsilon} \right) \frac{\pi}{z} [\delta_{kx} a_x(\xi, \varphi_\xi) - \delta_{ky} a_y(\xi, \varphi_\xi)] \right\}, \quad (47c)$$

where we left the ν -dependent terms separated from the others, for easy identification. One ν -dependent term comes from a TST contribution, identified by the h_{zz} function in Eq. (47a), and the other comes from the sum of ST and TS contributions, which are equal in magnitude, identified by the factor 2 and the function a_z in Eq. (47a).

All the tensorial properties of the TERS scattering of mode η are contained in $\mathcal{J}^{(\eta)}$, appearing in Eq. (19). Deriving the following final form for each mode from Eq. (47) is tedious, so we do it in Appendix D, and reproduce the result as a function of q and z below,

$$\tilde{\mathcal{J}}^{(A_1)}(q; z) = (2\pi)^3 |\bar{\alpha}^{(A_1)}|^2 |E_z(\omega)|^2 \left\{ |g_z^{\text{FF}}|^2 \left| \left(\frac{r_{\text{tip}}^3 f_e}{2n^2} \right)^2 \frac{9}{384} \left[\frac{2q^3 K_3(qz)}{z} - q^4 K_2(qz) \right] \right. \right. \\ \left. \left. + \nu \left(\frac{r_{\text{tip}}^3 f_e}{2n^2} \right)^2 \left[\frac{9}{384} q^4 K_4(qz) - \frac{6}{48} \frac{q^3 K_3(qz)}{z} + \frac{1}{8} \frac{q^2 K_2(qz)}{z^2} \right] \right. \right. \\ \left. \left. + 2\nu \left(\frac{r_{\text{tip}}^3 f_e}{2n^2} \right) q e^{-qz} \right|^2 \right. \\ \left. + |g_{\parallel}^{\text{FF}}|^2 \left| \left(\frac{r_{\text{tip}}^3 f_e}{2n^2} \right) q e^{-qz} \right|^2 \right\}, \quad (48a)$$

$$\mathcal{J}^{(E_{2g})}(q; z) = (2\pi)^3 |\bar{\alpha}^{(E_{2g})}|^2 |E_z(\omega)|^2 \left\{ |g_z^{\text{FF}}|^2 \left| \left(\frac{r_{\text{tip}}^3 f_e}{2n^2} \right)^2 \left(\frac{9}{384} \right) q^4 K_2(qz) \right|^2 \right. \\ \left. + 2 |g_{\parallel}^{\text{FF}}|^2 \left| \left(\frac{r_{\text{tip}}^3 f_e}{2n^2} \right) q e^{-qz} \right|^2 \right\}, \quad (48b)$$

where we used $\alpha_{zz}^{\text{tip}} = 2\pi\varepsilon_0 r_{\text{tip}}^3 f_e$ [10] and $\mathcal{J}^{(E_{2g})}(q; z) = \mathcal{J}^{(E_{2g},x)}(q; z) + \mathcal{J}^{(E_{2g},y)}(q; z)$, assuming that L_c is the same for the two branches of mode E_{2g} . Note that there are factors that

are powers of $r_{\text{tip}}^3 f_e / (2n^2)$ defining the strength of each contribution to the TERS near field intensity. The tip radius r_{tip} will enter the tip-sample distance z , so it affects the result in more than one way, but f_e and n only appear in the mentioned factor. This means that they can be joined into a single parameter

$$f_e^{\text{eff}} \equiv f_e / n^2, \quad (49)$$

which behaves as an effective tip enhancement factor modified by the medium refractive index, and the factors in Eq. (48) can be rewritten according to $r_{\text{tip}}^3 f_e / (2n^2) \rightarrow r_{\text{tip}}^3 f_e^{\text{eff}} / 2$.

From Eq. (19), the TERS signal of mode η is the internal product between $\mathcal{J}^{(\eta)}$ and the L_c dependent correlation function $\mathcal{L}^{(\eta)}$. In Fig. 2 (a)–(c) we plot the TERS intensity for modes A_1 and E_{2g} for a variety of ν values (note that only A_1 depends on ν), as a function of the tip-sample distance, as is done in tip approach experiments [8, 11, 24], with fixed L_c , r_{tip} and f_e , and write on the top of the plot the values used. In Fig. 2 (d) we fix ν , r_{tip} and f_e , and plot the curves for a variety of L_c values. As in Fig. 1, we call z_{tip} the distance from the sample surface to the tip point, which is the quantity in the horizontal axis of the plots, such that $z = z_{\text{tip}} + r_{\text{tip}}$ is the position of the dipole inside the tip that we use to model the field emitted by it. In Fig. 2 (a) and (b) all the curves are normalized within themselves, with the reference at the closest point at which the tip gets to the sample, which we take at $z_{\text{tip}} = z_0 = 5$ nm [see Fig. 1]. In Fig. 2 (c) and Fig. 2 (d) we compare the absolute intensity of the curves, and for that we take the A_1 near field TERS intensity with $\nu = 0$ and $L_c = 0$ nm at $z_{\text{tip}} = 5$ nm as unity, and we do not plot E_{2g} because its intensity in relation to A_1 can change from material to material.

We see in Fig. 2 (a) and (b) that increasing ν increases the distance between the A_1 and E_{2g} curves, for both $L_c = 0$ nm and $L_c = 15$ nm. It does not act alone, though, since a higher L_c yields a higher impact of ν . Most strikingly, in Fig. 2 (c), an increase in ν dramatically increases the intensity of the near field TERS signal. This means means that the z axis sample Raman response can have a significant impact on the TERS enhancement. Note in Fig. 2 (d) that as L_c increases the absolute value of the near field TERS intensity decreases (the plot displays only the A_1 mode, but for E_{2g} the same behavior appears). For the E_{2g} mode this is expected due to the scattering destructive interference arising from the phonon symmetry, but it seems counter-intuitive for the A_1 mode, which displays constructive interference instead [10], hinted in the Raman tensors of Eq. (16). This behavior

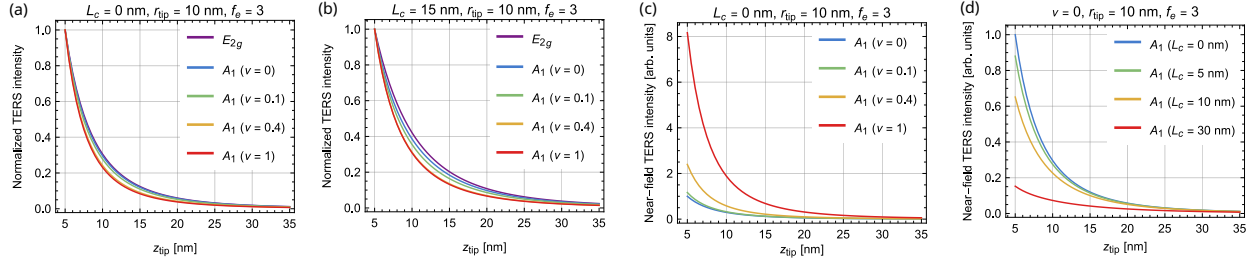


FIG. 2. (a)–(b) Normalized TERS intensity according to Eq. (19) and Eq. (48) for modes A_1 and E_{2g} for a variety of ν values, as a function of the tip-sample distance, with fixed L_c , r_{tip} and f_e . (c)–(d) Absolute value of the near field TERS intensity according to Eq. (19) and Eq. (48) for mode A_1 , where in (c) we show a variety of ν values, while in (d) curves for different L_c are shown, for fixed r_{tip} and f_e . The fixed values within each plot are written on top of each frame. According to Fig. 1, we call z_{tip} the distance from the sample surface to the tip point, which is the quantity in the horizontal axis of the plots, such that $z = z_{\text{tip}} + r_{\text{tip}}$ is the value used in Eq. (48).

follows from the norm of \mathcal{L} being proportional to $1/L_c^2$, together with the fact that the TERS signal can be put in the form of an internal product with \mathcal{L} , as mentioned in Sec. III. One could imagine that this is particular of our choice for a Gaussian \mathcal{L} , but a different unit integral function such as the sinc function, $\mathcal{L}(\rho; L_c) = 2(\pi L_c)^{-2} \text{sinc}[(\rho/L_c)^2]$, has norm $2/(\pi^2 L_c^2)$, showing the same behavior as the Gaussian. Detailed discussions of the influence of the physical parameters in the TERS measurements follow in Sec. VII.

VII. DISCUSSION

The discussion is split into three parts, Sec. VII A to discuss the normalized TERS measurements, as those in Fig. 2 (a) and 2 (b), Sec. VII B to discuss enhancement measurements, affected by the absolute intensity of the near field, as in Fig. 2 (c) and 2 (d), and Sec. VII C to address the implications of the out-of-plane response to the fitting of graphene measurements.

A. Normalized TERS measurements

In normalized TERS measurements, as those in Fig. 2 (a) and 2 (b), it is the distance between the E_{2g} and A_1 curves that testifies the difference in steepness between the tip approach curves of the two modes [7, 10, 11]. With that in mind, we construct a figure of merit based on the integral of the normalized tip approach curve of each mode between points z_1 and z_2 ,

$$\mathcal{W}^{(n)}(z_1, z_2) \equiv \frac{\int_{z_1}^{z_2} S^{(n)}(\mathbf{r}_0, \omega_s; z) dz}{S^{(n)}(\mathbf{r}_0, \omega_s; z_1)}. \quad (50)$$

We always pick $z_1 = z_0 + r_{\text{tip}}$, and a z_2 large enough so the two curves practically match each other, in particular $z_2 = z_0 + r_{\text{tip}} + 100$ nm. The figure of merit is the difference between the integrals of the two modes,

$$\Delta\mathcal{W} \equiv \mathcal{W}^{(E_{2g})}(z_1, z_2) - \mathcal{W}^{(A_1)}(z_1, z_2), \quad (51)$$

or equivalently the area between the two curves, being positive when E_{2g} is most of the times above A_1 , which is the standard situation. The larger $\Delta\mathcal{W}$, the more noticeable is the difference between the E_{2g} and A_1 curves.

In Fig. 3, we plot 2D maps of $\Delta\mathcal{W}$ for different pairs of parameters in our model, Eq. (19) and (48), namely the coherence length L_c , the material out-of-plane relative response ν , the tip radius r_{tip} , the tip response factor f_e , and the ratio of the far field propagation factors $g_R \equiv g_z^{\text{FF}}/g_{\parallel}^{\text{FF}}$. The parameters L_c and ν are characteristics of the material, while r_{tip} , f_e and g_R vary with the experimental settings. The values for the fixed parameters in all plots are $L_c = 0$ nm, $\nu = 0$, $r_{\text{tip}} = 7$ nm, $f_e = 3$, and $g_R = 1$, except when they are varied, with $z_0 = 5$ nm in all plots without exception. In Eq. (48) there is also a dependence on the refractive index n of the medium between tip and sample, but with the definition of Eq. (49), the refractive index enters as a modification of f_e , leading to an effective f_e^{eff} . Therefore we do not plot the n dependence explicitly, and the effect of n is obtained by interpreting f_e as f_e^{eff} . Notice that g_z^{FF} and $g_{\parallel}^{\text{FF}}$, and consequently g_R , depend on how much of the scattered light in each polarization the optical system is able to collect and direct towards the detectors. Also, because g_R is a ratio, we plot $\log_2(g_R)$ to have a balanced representation of $g_R > 1$ and $g_R < 1$. Importantly, we use the same \log_{10} color scale for $\Delta\mathcal{W}$ across all plots of Fig. 3, and the contours are separated by $10^{1/4}$ [arb. units] in all of them.

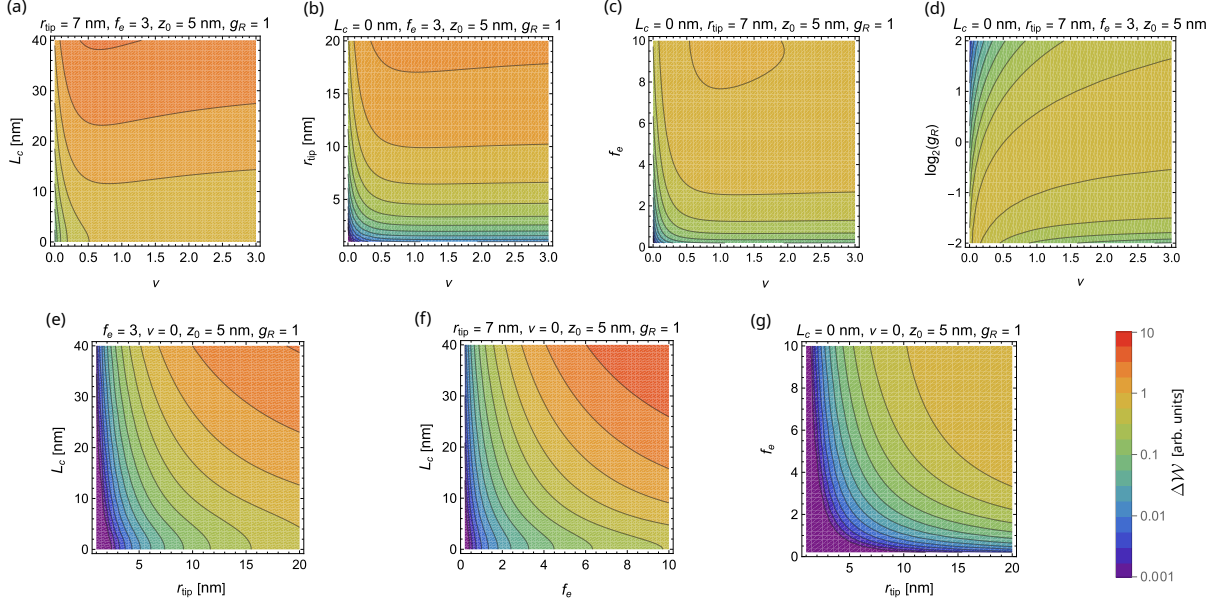


FIG. 3. Plots of the figure of merit $\Delta\mathcal{W}$, defined by Eq. (50) and (51), which quantifies the difference under the normalized tip approach curves between modes A_1 and E_{2g} . In each of the plots, a pair of physical parameters in the model is varied, while the others are fixed. The varied parameters encompass the coherence length L_c , the material out-of-plane relative response ν , the tip radius r_{tip} , the tip response factor f_e , and the ratio of the far field propagation factors $g_R = g_z^{\text{FF}}/g_{\parallel}^{\text{FF}}$, of which we plot $\log_2(g_R)$. We use $z_0 = 5$ nm in all plots, and the values for the fixed parameters in each plot appear written above each one respectively. We use the same \log_{10} color scale for $\Delta\mathcal{W}$ across all plots, and the contours are separated by $10^{1/4}$ [arb. units] in all of them.

At first glance, it is noticeable that the plots with L_c [Fig. 3 (a), 3 (e) and 3 (f)] are the ones with the highest values of $\Delta\mathcal{W}$, meaning that a large L_c is the single most determinant factor to a large separation between the two curves. This is attributed to a larger destructive interference in the sample scattering pattern of the E_{2g} mode when the coherence length is large [10, 11].

When $L_c = 0$ nm, the highest values of $\Delta\mathcal{W}$ occur for $\nu > 0.5$ combined with a large r_{tip} [Fig. 3 (b)]. Also note significantly that, when varying ν , $\Delta\mathcal{W}$ plateaus from $\nu \approx 1$ onwards, and for $\nu > 1$ there is just a slight decrease in $\Delta\mathcal{W}$ for all variables except g_R [Fig. 3 (a)–(d)]. For $\log_2(g_R) \approx 0$ ($g_R \approx 1$) with high ν it might seem that $\nu > 1$ still has a significant impact in the growth of $\Delta\mathcal{W}$ [Fig. 3 (d)], but note that in this plot $\Delta\mathcal{W} < 1$

[arb. units] everywhere, being lower than all other ν plots [Fig. 3 (a)–(d)]. We interpret this as g_R being the least important parameter in the variation of $\Delta\mathcal{W}$.

When it comes to the refractive index n , its variation is here interpreted as a rescaling of f_e in Eq. (48) according to Eq. (49). For instance, in a medium where $n = 3$ one has $f_e^{\text{eff}} = f_e/9$, so if $f_e = 4$ in a TERS setting with air between sample and tip, we would have $f_e^{\text{eff}} = 0.44$. As a rule of thumb, the larger is n , the smaller is f_e^{eff} , and this means a smaller $\Delta\mathcal{W}$ [Fig. 3 (c), (f) and (g)]. The intuition behind this is that a large n causes the optical path of the field in the region between the sample and the tip to be large, so the near field becomes weaker and the difference between the normalized curves decreases significantly.

B. TERS enhancement measurements

The effect of ν and g_R are much more pronounced in non-normalized measurements, because they can significantly increase the scattered field intensity for small tip-sample distances, as seen in Eq. (48) and Fig. 2 (c). When trying to model this kind of measurement, we need additional parameters, namely the intensity of the field when the tip is distant from the sample (“tip up” setting), corresponding to the scattered Raman far field $S_{\text{FF}}^{(\eta)}$ for mode η . We need to specify $S_{\text{FF}}^{(\eta)}$ in relation to the field intensity for a small tip-sample distance (“tip down” setting) for each mode, that is including the near field, and we also need to compare the values between E_{2g} and A_1 modes. To do that, we use

$$S_{\text{total}}^{(\eta)}(z) = S_{\text{NF}}^{(\eta)}(z) + S_{\text{FF}}^{(\eta)}, \quad (52)$$

where $S_{\text{NF}}(z)$ is the scattered field intensity calculated in Eq. (19), which depends on the tip-sample distance z , and $S_{\text{FF}}(z)$ is the scattered far field intensity, which is independent of z .

The insightful experimental physical quantity in this framework is the TERS spectral enhancement, which is the intensity of the scattered Raman signal when the tip is engaged in the sample in relation to when it is far from the sample (intensity at “tip down” divided by intensity at “tip up”), defined by

$$E^{(\eta)} \equiv \frac{S_{\text{total}}^{(\eta)}(z_0 + r_{\text{tip}})}{S_{\text{total}}^{(\eta)}(z_0 + r_{\text{tip}} + z_F)}, \quad (53)$$

with $z_F \gtrsim 10z_0$. When z_F is large enough, $S_{\text{total}}^{(\eta)}(z_0 + r_{\text{tip}} + z_F) \approx S_{\text{FF}}^{(\eta)}$, so we can write

$$E^{(\eta)} \approx \frac{S_{\text{NF}}^{(\eta)}(z_0 + r_{\text{tip}})}{S_{\text{FF}}^{(\eta)}} + 1. \quad (54)$$

In Fig. 4 we plot the tip approach intensity $S_{\text{total}}^{(\eta)}(z)$ for the two modes in solid lines, and in dashed lines we plot the far field intensity $S_{\text{FF}}^{(\eta)}(z)$ that we have used. The intensities used are $S_{\text{FF}}^{(A_1)} = (1/10)S_{\text{NF}}^{(A_1)}(z_0 + r_{\text{tip}})|_{L_c=0}$, with $z_0 = 5$ nm and $r_{\text{tip}} = 7$ nm, and for E_{2g} we use $S_{\text{FF}}^{(E_{2g})} = (2/3)S_{\text{FF}}^{(A_1)}$, which yield $E^{(E_{2g})} = 5.0$ and $E^{(A_1)} = 10.5$. These values are chosen because they are close to the ones appearing in an MoSe₂ experiment [25]. The other parameters of the plot in Fig. 4 are $L_c = 0$ nm, $f_e = 3$, $\nu = 1$ and $g_R = 1$.

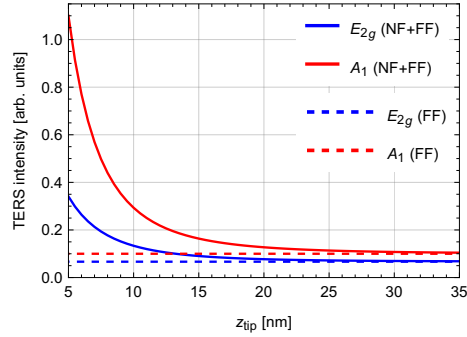


FIG. 4. Construction of the total TERS intensity (solid lines), according to Eq. (52), comprised of the contribution of the near field TERS (NF), calculated with Eq. (19), and a far field (FF) intensity constant along z_{tip} (dashed lines). In the plot we use, for A_1 mode (red lines), $S_{\text{FF}}^{(A_1)} = (1/10)S_{\text{NF}}^{(A_1)}(z_0 + r_{\text{tip}})|_{L_c=0}$, with $z_0 = 5$ nm and $r_{\text{tip}} = 7$ nm, and for E_{2g} (blue lines) we use $S_{\text{FF}}^{(E_{2g})} = (2/3)S_{\text{FF}}^{(A_1)}$. For both modes we use $L_c = 0$ nm, $f_e = 3$, $\nu = 1$ and $g_R = 1$.

The figure of merit to relate the two modes is the ratio $E^{(A_1)}/E^{(E_{2g})}$ of the enhancement of the A_1 mode to that of E_{2g} , which for the plot in Fig. 4 is $E^{(A_1)}/E^{(E_{2g})} = 2.1$. In Fig. 5 we plot $E^{(A_1)}/E^{(E_{2g})}$ with varying parameters, analogously to what we did to $\Delta\mathcal{W}$ in Fig. 3. We use the same far field Raman intensity of A_1 mode in all plots, namely $S_{\text{FF}}^{(A_1)} = (1/10)S_{\text{NF}}^{(A_1)}(z_0 + r_{\text{tip},0})|_{L_c=0}$, with $z_0 = 5$ nm and $r_{\text{tip},0} = 7$ nm, and for E_{2g} we use $S_{\text{FF}}^{(E_{2g})} = (2/3)S_{\text{NF}}^{(A_1)}$, as in Fig. 4. These serve just as reference values, not playing a significant role in the tendencies shown in Fig. 5.

As we expected, in the plots of Fig. 5 it is evident that a large ν implies a large $E^{(A_1)}/E^{(E_{2g})}$, as the maximum enhancement ratio in the ν -dependent plots [Fig. 5 (a)–(d)]

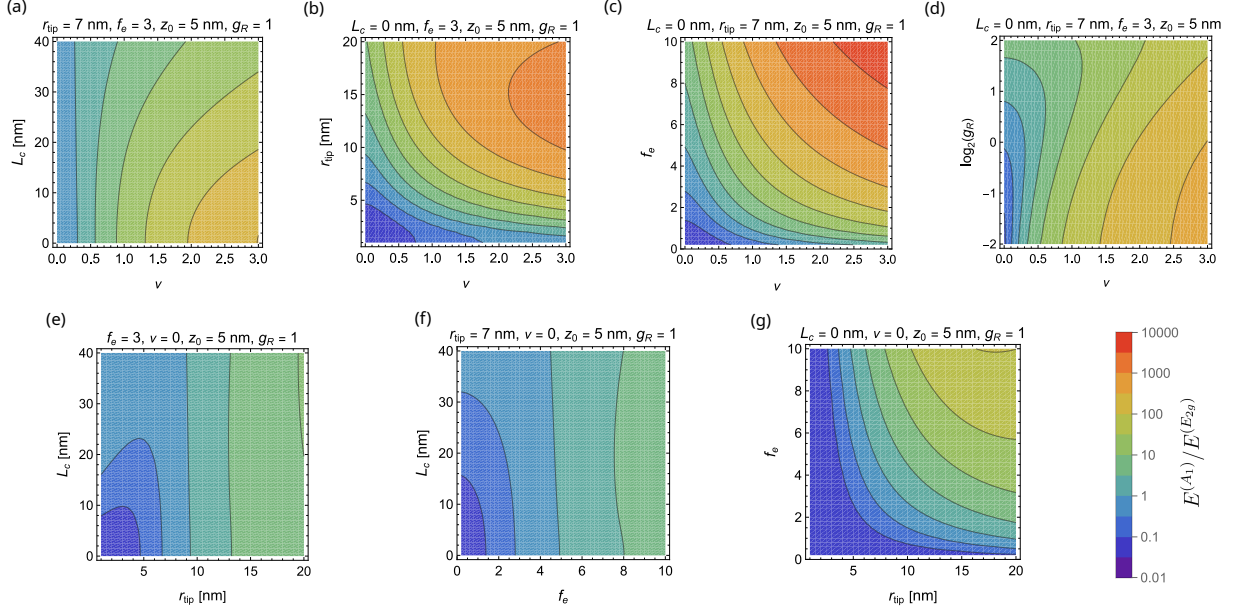


FIG. 5. Plots of the enhancement ratio $E^{(A_1)}/E^{(E_{2g})}$, constructed from the enhancements defined in Eq. (53). In each of the plots, a pair of physical parameters in the model is varied, while the others are fixed. The varied parameters encompass the coherence length L_c , the material out-of-plane relative response ν , the tip radius r_{tip} , the tip response factor f_e , and the ratio of the far field propagation factors $g_R = g_z^{\text{FF}}/g_{\parallel}^{\text{FF}}$, of which we plot $\log_2(g_R)$. In all plots we use $z_0 = 5$ nm, the far field intensities for the A_1 mode $S_{\text{FF}}^{(A_1)} = (1/10)S_{\text{NF}}^{(A_1)}(z_0 + r_{\text{tip},0})|_{L_c=0}$, where $r_{\text{tip},0} = 7$ nm, and for E_{2g} we use $S_{\text{FF}}^{(E_{2g})} = (2/3)S_{\text{NF}}^{(A_1)}$. The values for the fixed parameters in each plot appear written above each one respectively. We use the same \log_{10} color scale for $E^{(A_1)}/E^{(E_{2g})}$ across all plots, and the contours are separated by $10^{1/2}$ in all of them.

is always larger than in the $\nu = 0$ plots [Fig. 5 (e)–(g)]. In addition, f_e is the most important factor which, associated with a large ν , leads to a large enhancement ratio [Fig. 5 (c)], because it increases the TERS intensity, as evident in Eq. (48). The tip radius r_{tip} is also important, as it follows f_e in Eq. (48), but since it also means a higher $z = z_0 + r_{\text{tip}}$ distance, at some point its increase starts to lower $E^{(A_1)}/E^{(E_{2g})}$ [Fig. 5 (b)].

Note that increasing L_c leads the enhancement ratio $E^{(A_1)}/E^{(E_{2g})}$ towards unity, that is, a balanced enhancement between the two modes. In Fig. 5 (a), where for large ν the ratio is larger than unity, increasing L_c decreases the enhancement ratio, while in Fig. 5 (e) and 5 (f), where the ratio is smaller than unity for small r_{tip} and f_e , increasing L_c increases the

ratio. This is explained by the behavior of our correlation function model, as presented in Sec. III and seen in Fig. 2 (d), that causes the TERS near field intensity to decrease as L_c increases [in Fig. 2 (d) only A_1 mode is shown, but the E_{2g} behavior is analogous]. Because the far field is fixed and independent of L_c , if the near field decreases for both A_1 and E_{2g} modes, then both enhancements decrease, causing the enhancement ratio $E^{(A_1)}/E^{(E_{2g})}$ to get closer to unity.

There are regions in the parameters space in which the ratio is smaller than unity, meaning that the E_{2g} enhancement is larger than A_1 . These regions are those for very small parameters, and appear more strikingly in Fig. 5 (g) in which at least three of the parameters f_e , r_{tip} , L_c and ν are small at the same time, suppressing the intensity of A_1 more than of E_{2g} .

A word must also be said concerning the tip radius as an enhancement factor. In the model (see Sec. V and Ref. [10]), the tip is a spherical body which originates a dipole emission pattern in response to the external electric field [26]. This means that the response of the tip depends on its volume, which is where the r_{tip}^3 factors in Eq. 48 come from. Therefore, even though a larger tip means that the distance of the oscillating effective dipole inside the tip is farther from the sample, this can be compensated by a stronger response due to the larger dipole volume, and thus a large r_{tip} , in the current model, can be associated with a larger enhancement. Note however that there is a limit to this, and for some parameters increasing r_{tip} starts to decrease the enhancement, as seen in Fig. 5 (b) for large ν .

It is important that ν should be apparent only in TMDs, which have a strong out-of-plane Raman response $\nu \sim 1$, in contrast to the weak graphene response $\nu \ll 1$.

C. Graphene TERS experiments

The discussion in Sec. VII A leads to the prediction that a very large separation between E_{2g} and A_1 normalized tip approach curves will inevitably need $L_c > 0$ to be modelled. Curves with a smaller separation, on the other hand, can be modelled with $L_c = 0$ as long as ν , r_{tip} , f_e , or some combination of them are large. In Fig. 6 we show an example of this on data from Ref. [11] [Fig. 6 (a) and 6 (b)] and Ref. [8] [Fig. 6 (c)], which perform tip approach TERS experiments with graphene. In the three plots, light blue dots represent the normalized tip approach experimental data from E_{2g} mode, orange triangles are data from

A₁ mode, and the light blue and orange solid thin lines are a fitting using our own model, but with the parameters provided in the respective original papers, all with $L_c > 0$. The original parameters for Ref. [11] are $L_c = 40$ nm, $r_{\text{tip}} = 15$ nm and $f_e = 4$, and those for Ref. [8] are $L_c = 13$ nm for mode E_{2g}, $L_c = 10$ nm for mode A₁, $r_{\text{tip}} = 8$ nm and $f_e = 2$, and with $\nu = 0$, $g_R = 1$ and $z_0 = 5$ nm for both. It should be noted that in the data from Ref. [11] the two mode curves are much more separated than those from Ref. [8], so the first needs a much larger L_c in their fit than the latter, in accordance with our conclusion that a large L_c is needed for widely separated curves.

To investigate the necessity of TERS coherence length in the explanation of the experimental results, we first try to fit the data from Ref. [11] with $L_c = 0$. These are the thicker solid ($\nu = 0.1$) and dashed ($\nu = 1$) blue (E_{2g}) and red (A₁) curves in Fig. 6 (a). As shown in the plot, $\nu = 0.1$ cannot reach the measured separation between the curves when $L_c = 0$. If one goes to $\nu = 1$, the curve separation can be enlarged significantly, while the smallest tip-sample separation z_0 has to be set to 8 nm for the appropriate curve decay, but this is still not enough. On top of that, $\nu = 1$ is unphysical, since for graphene $\nu \ll 1$.

In Fig. 6 (b), we abandon the restriction of $L_c = 0$. Our results of Fig. 3 can be used as a guide to a fit similar to that of Ref. [11], but with a smaller L_c . The plots in Fig. 3 (e) and 3 (f) indicate that the same $\Delta\mathcal{W}$ can be achieved, given a decrease in L_c , by an increase in r_{tip} or f_e , and we increase both, as well as set $\nu = 0.1$. However, our figure of merit only captures the area between the curves, and not the absolute position of the curves, associated with the decay rate in the tip approach. We are able to keep a similar $\Delta\mathcal{W}$ as in Ref. [11] for $L_c = 25$ nm if we use a larger $r_{\text{tip}} = 30$ nm and $f_e = 5.5$, but to place the curves in the appropriate position, we must use a larger $z_0 = 8$ nm (solid lines). With $z_0 = 5$ nm (dashed lines) the curves decay too fast and pass below the data, and increasing z_0 raises the curves, since it is probing a region with a weaker near field. This means that the results of Ref. [11] can also be explained by a model with a significantly smaller coherence length than assumed in their article, as long as there are strong enhancing factors present, such as a larger r_{tip} , f_e , and ν .

Importantly, note that the engaging distance z_0 may be seen as a restriction on the parameters range, in the sense that $L_c = 20$ nm can only fit the data if $z_0 > 10$ nm, which is incompatible with the TERS setting used in the experiment. It must be stressed that a large L_c making the curves less steep is in accordance with the increase in L_c causing a

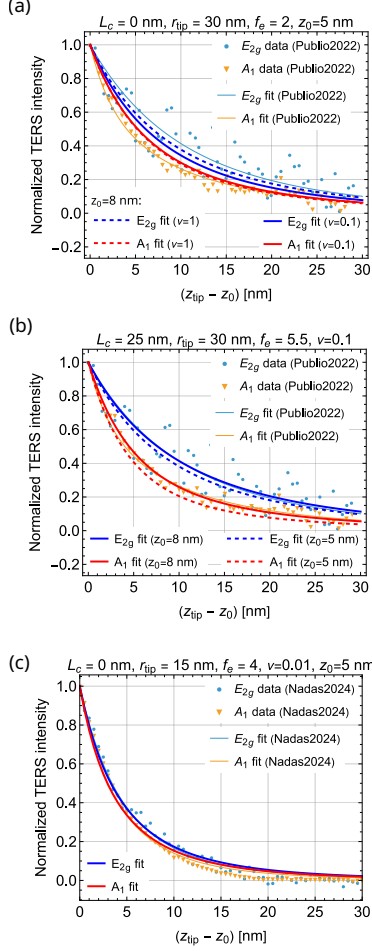


FIG. 6. Comparison between experimental TERS tip approach data collected in Ref. [11] and [8], the theoretical fitting of the original articles, and the fitting according to our theory, Eq. (19) and (48). Across all plots, light blue dots represent E_{2g} mode data, inverted orange triangles are A_1 , a light blue (orange) solid line is a fit with our theory using the fitting parameters of the original articles for E_{2g} (A_1) mode, and a dark blue (red) solid line is the fit for E_{2g} (A_1) mode with new parameters. In (a), data from Ref. [11] is fit with $L_c = 0$, both with $\nu = 0.1$ and $z_0 = 5$ nm (solid line), and with $\nu = 1$ and $z_0 = 8$ nm (dashed line). In (b) we use $L_c = 25$ nm, with $z_0 = 8$ nm (solid line) and $z_0 = 5$ nm (dashed line). In (c) data from Ref. [8] is fit with $L_c = 0$ and a negligible $\nu = 0.01$. The remaining parameters used in the fittings are written on top of each respective plot.

decrease in the overall TERS intensity of both modes, discussed in Sec. VI. So L_c and z_0 go together in decreasing the steepness of the curves, such that to fit the same data with a smaller L_c , an increase in z_0 is necessary in compensation. In a nutshell, the wide separation

between the curves demands some combination of large enhancing factors, be it r_{tip} , f_e or ν , while the restriction $z_0 \leq 8$ nm sets $L_c \gtrsim 25$ nm. The more one knows the experimental parameters, the tighter the restriction on a measurement of L_c .

In Fig. 6 (c), with data from Ref. [8], because the curves are close, we can model them with $L_c = 0$, namely with $\nu = 0.01$ (which is indistinguishable from the same curve with $\nu = 0$).

We can conclude from this that the TERS measurements with the graphene sample from Ref. [11] need $L_c > 0$ even in our new model that includes the out-of-plane response ν , while measurements in the sample from Ref. [8] do not and can be explained with $L_c = 0$. This behavior might have several causes which we cannot infer from the tip approach curves alone, possibly the influence of local doping [27], or some other feature affecting the coherence length. The data from Ref. [8], shown in Fig. 6 (c), is the average of many experiments, and it thus shows a smaller fluctuation, but we believe that the difference is too large to stem from this fact alone. In either case, it seems that ν can be neglected in fittings of TERS measurements on graphene.

VIII. CONCLUSION

We have presented an extension of the TERS theoretical model to include the out-of-plane Raman response of 2D materials, a necessary step if the model is applied to TERS measurements on TMDs. On top of that, we could write the TERS near field intensity as an internal product between two functions, one having propagation and mode symmetry information, which could be written in exact analytical form, and the other having polarizability coherence length information. The most important advantages of this interpretation are two. One is that it is easy to calculate numerically, because it departs from analytical expressions. The other is that it is now possible to easily experiment with different polarizability correlation functions. We have shown that the model is sensitive to the choice of the correlation function, and this choice may influence how L_c changes the TERS measurements. So it is crucial to proceed with a deeper theoretical investigation on these functions, and having a cheap computational tool to test them will be essential. Our model also points a way to investigate the valid correlation functions experimentally, as an isolated manipulation of L_c , for instance with a manipulation of the doping in the sample [27], could sort this question

out.

An extensive analysis of how the physical parameters in the model change the predictions for experimental measurements was also made. This analysis, summarized in Fig. 3 and 5, can serve as a useful guide in the fitting of TERS experimental data, as we did in the fittings of Fig. 6. Because the model is too complex with a very large number of physical parameters, having an intuition of how the change in the parameters changes the model output is essential to avoid unrealistic fittings. It also shows, importantly, that a strong TERS enhancement is a necessary condition for investigating the physics of a TERS sample, which means surveying the difference in TERS signals, here represented by differences in tip approach curves. Whether the enhancement is due to a large factor f_e , a large tip radius, a large relative Raman response ν , or bringing the tip really close to the sample, the stronger the enhancement, the better one is able to distinguish the effect of a physical parameter on different Raman peaks, for instance the coherence length L_c .

In particular, we show that the coherence length L_c is the most important factor to get a large separation between normalized tip approach TERS curves of A_1 and E_{2g} modes, an effect of the destructive interference in the signal of the E_{2g} mode [10], consistent with the results of Ref. [28]. This means that any data in which the curves have a large separation will demand $L_c > 0$, while closer curves might be fitted with $L_c = 0$, which reinforces the importance of the normalized TERS curves comparison as a testifier of $L_c > 0$ in the sample [7, 10], especially in graphene, in which $\nu \approx 0$.

It also comes out from our analysis that a large out-of-plane Raman response ν in the sample implies a large enhancement ratio between modes A_1 and E_{2g} , since only mode A_1 depends on ν and thus a large ν increases the difference in the enhancements. In addition, the most important factor to increase the enhancement ratio is the tip enhancement factor f_e , also consistent with Ref. [28], because it dramatically increases the TST term, which increases more for the A_1 mode, and if it is associated with $\nu \geq 1$ it leads to very high enhancement ratios. In turn, an increase in L_c drives the enhancement ratio towards unity, which is a feature of the model predicting a decrease in the absolute TERS signal of both modes as L_c increases.

A comparison with experimental data shows that the model is sound and can fit them with reasonable physical parameters. However, there are still aspects that must be investigated, as in the data from Fig. 6, in which graphene measurements from Ref. [11] demand a

coherence length $L_c > 0$, while those from Ref. [8] can be fit with $L_c = 0$. The origin of L_c is still elusive, whether it stems from the isolated phonon dynamics or from a coupled dynamics induced by the electric field, and the present model will be useful to address future measurements, possibly on TMDs, to compare with the previous literature [8, 11].

ACKNOWLEDGMENTS

The authors acknowledge Denis Basko for helpful discussions. This work was supported by Conselho Nacional de Desenvolvimento Científico e Tecnológico (CNPq, Grants No. 408697/2022-9, and No. 421469/2023-4), and Fundação de Amparo à Pesquisa do Estado de Minas Gerais (FAPEMIG, Grants No. APQ-04852-23, and No. RED-00081-23).

Appendix A: Focused radially polarized Gaussian beam

In TERS experiments, a radially polarized Gaussian beam is focused on the tip in order to obtain a large electric field component along the tip axis. The tip is especially sensitive to this component, which results in a large field being scattered from the tip to the sample in the TST and ST terms. In the TS term, the sample responds directly to the incident field, so if the sample Raman tensor has a z component, it might contribute significantly to the TERS signal. We provide, in this appendix, a justification for why the component of the focused field parallel to the xy sample plane can be ignored in our treatment.

A radially polarized Gaussian doughnut mode on plane xy propagating in the z direction, after focusing, is [3]

$$\mathbf{E}(r, \phi_r, z) = -\frac{ikf^2}{2cw_0} \sqrt{\frac{n_1}{n_2}} E_0 e^{-ikf} \begin{bmatrix} iI_r(r, z) \cos \phi_r \\ iI_r(r, z) \sin \phi_r \\ -I_z(r, z) \end{bmatrix}, \quad (\text{A1})$$

where (r, ϕ_r) are radial coordinates at the xy plane, k is the beam wave vector amplitude, w_0 is the Gaussian beam waist before focusing, f is the objective lens focal distance, n_1 and n_2 are the refractive indices before and after the lens, respectively, and

$$I_r(r, z) = 4 \int_0^{\theta_{\max}} f_w(\theta) (\cos \theta)^{-1/2} (\sin \theta)^2 \times \cos \theta J_1(kr \sin \theta) e^{ikz \cos \theta} d\theta, \quad (\text{A2a})$$

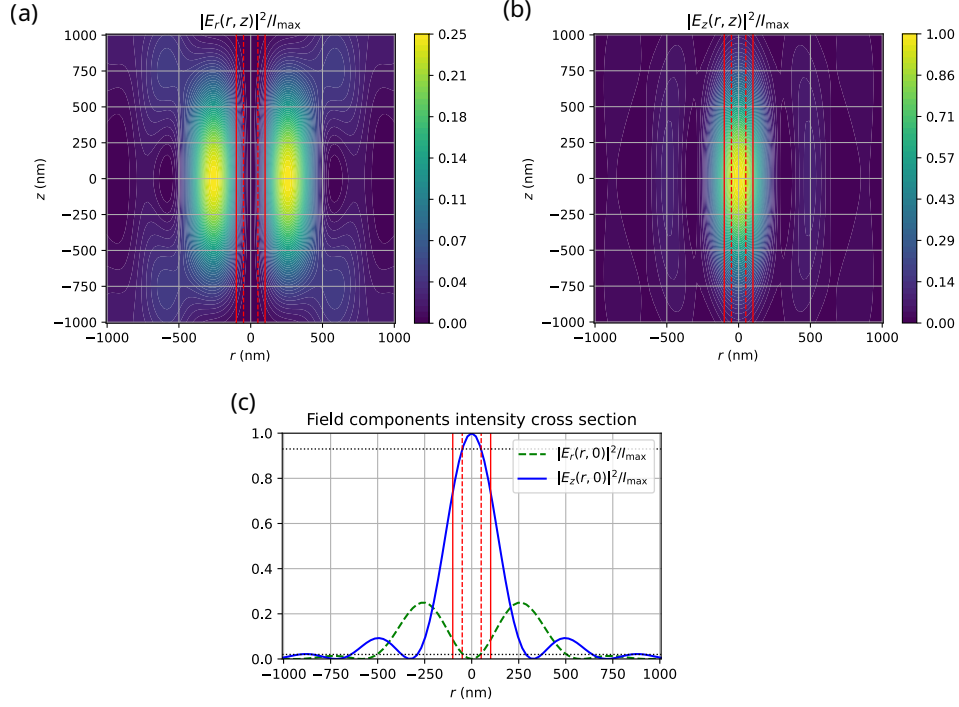


FIG. 7. Intensity of components of the focused radially polarized Gaussian beam, all quantities normalized by the maximum field intensity, $I_{\max} \equiv |\mathbf{E}(0, 0)|^2$. In (a) we plot the radial component intensity and in (b) the z component intensity—note the difference in the color scale between the two plots. In (c), we plot a cross section of the field components intensities at $z = 0$. The vertical red lines mark a 50 nm (dashed line) and a 100 nm (solid line) radius around the beam axis, where the tip should be located. The horizontal black dotted lines mark the normalized intensities of 0.02 (bottom) and 0.93 (top), marking the respective values of the r and z components at the 50 nm radius.

$$I_z(r, z) = 4 \int_0^{\theta_{\max}} f_w(\theta) (\cos \theta)^{-1/2} (\sin \theta)^2 \times \sin \theta J_0(kr \sin \theta) e^{ikz \cos \theta} d\theta, \quad (\text{A2b})$$

where θ_{\max} is the largest polar angle captured by the lens (related to the NA by $\text{NA} = n_2 \sin \theta_{\max}$), and

$$f_w(\theta) = e^{-\frac{1}{f_0^2} \frac{\sin^2 \theta}{\sin^2 \theta_{\max}}}, \quad (\text{A3a})$$

$$f_0 = \frac{w_0}{f \sin \theta_{\max}}. \quad (\text{A3b})$$

In Fig. 7 (a) and (b) we plot the intensity of the parallel and perpendicular components of the field in the rz plane, calculated numerically from Eq. A2, normalized by the maximum intensity of the perpendicular field. In Fig. 7 (c) we plot the intensity of the perpendicular (z , blue solid line) and radial (r coordinate, or xy plane, green dashed line) field components at the beam waist, $z = 0$, normalized by the highest possible intensity. The plot parameters that we use are a laser wavelength of $\lambda = 632.8$ nm, yielding $k = 9.93 \times 10^{-3}$ rad/nm, laser beam waist width $w_0 = 10$ mm, objective lens focal distance $f = 170$ μ m, objective NA 1.4, and refractive index of medium after the lens (same as glass) $n = 1.52$. These parameters result in a maximum lens angle $\theta_{\max} = 33.5^\circ$, or $\sin \theta_{\max} = 0.92$, from $\text{NA} = n \sin \theta_{\max}$, and $f_0 = 64$. Note that A2 is a function of kr , so Fig. 7 can be easily adapted to other wavelengths by rescaling the axes.

The tip and sample are placed as close as possible to the beam waist at $z = 0$, where the field is strongest, and a shift of tens of nanometers above or below the z axis should not alter much this picture, as seen in Fig. 7 (a) and (b). The vertical red lines mark a 50 nm (dashed line) and a 100 nm (solid line) radius around the beam axis. If a 10 nm radius tip is well placed at the beam axis and aligned with it, it should be localized within the 50 nm radius and respond to the full E_z component. The horizontal black dotted lines in Fig. 7 (c) mark the normalized intensities of 0.02 and 0.93, marking the respective values of the r and z components at the 50 nm radius, meaning that, within this radius around the beam axis, $|E_r|^2 \lesssim 0.022|E_z|^2$. Even within a 100 nm radius, one has $|E_r|^2 \lesssim 0.13|E_z|^2$, so E_r can be quite safely neglected in comparison with E_z . In Ref. [11], it was considered that $|E_r|^2/|E_z|^2 \approx 1/3$, but we have shown that this ratio is at least 10 times smaller around the tip, where the near field is significant, so in the present article we only consider the z component of the incident field.

Appendix B: Angular integrals

We need to calculate three kinds of angular integrals,

$$I_{ij} = \int_0^{2\pi} \psi_j(\varphi_\varrho) \psi_i(\varphi_\varrho) e^{-i\xi\varrho \cos(\varphi_\xi - \varphi_\varrho)} d\varphi_\varrho, \quad (\text{B1a})$$

$$I_{iz} = \int_0^{2\pi} \psi_i(\varphi_\varrho) e^{-i\xi\varrho \cos(\varphi_\xi - \varphi_\varrho)} d\varphi_\varrho, \quad (\text{B1b})$$

$$I_{zz} = \int_0^{2\pi} e^{-i\xi\varrho \cos(\varphi_\xi - \varphi_\varrho)} d\varphi_\varrho, \quad (\text{B1c})$$

with $i, j \in \{x, y\}$, $\psi_x(\varphi_\varrho) = \cos(\varphi_\varrho)$, and $\psi_y(\varphi_\varrho) = \sin(\varphi_\varrho)$. We start with the most complicated one, Eq. (B1a). Expansion of the exponential with the Jacobi-Anger expansion [21] [see Eq. (32)] yields

$$\begin{aligned} I_{ij} &= \int_0^{2\pi} \psi_i(\varphi_\varrho) \psi_j(\varphi_\varrho) J_0(\xi\varrho) d\varphi_\varrho \\ &+ 2 \sum_{n=1}^{\infty} (-i)^n \int_0^{2\pi} \psi_j(\varphi_\varrho) \psi_i(\varphi_\varrho) \cos(n\varphi_\xi - n\varphi_\varrho) J_n(\xi\varrho) d\varphi_\varrho. \end{aligned} \quad (\text{B2})$$

We have three possible situations, $\psi_i(\varphi_\varrho) \psi_j(\varphi_\varrho) = \cos^2(\varphi_\varrho) = [1 + \cos(2\varphi_\varrho)]/2$; $\psi_i(\varphi_\varrho) \psi_j(\varphi_\varrho) = \sin^2(\varphi_\varrho) = [1 - \cos(2\varphi_\varrho)]/2$; or $\psi_i(\varphi_\varrho) \psi_j(\varphi_\varrho) = \sin(\varphi_\varrho) \cos(\varphi_\varrho) = \sin(2\varphi_\varrho)/2$. For compactness, we write $\mathcal{C}_{n\kappa} \equiv \cos(n\varphi_\kappa)$ and $\mathcal{S}_{n\kappa} \equiv \sin(n\varphi_\kappa)$, with $\kappa = \{\xi, \varrho\}$, and use the internal product definition $\langle f, g \rangle \equiv \int_0^{2\pi} f(\varphi_\varrho) g(\varphi_\varrho) d\varphi_\varrho$ to write

$$\begin{aligned} \int_0^{2\pi} \mathcal{C}^2(\varphi_\varrho) \mathcal{C}(n\varphi_\xi - n\varphi_\varrho) d\varphi_\varrho &= \langle (1 + \mathcal{C}_{2\varrho})/2, (\mathcal{C}_{n\xi} \mathcal{C}_{n\varrho} + \mathcal{S}_{n\xi} \mathcal{S}_{n\varrho}) \rangle \\ &= \mathcal{C}_{n\xi} (\langle 1, \mathcal{C}_{n\varrho} \rangle + \langle \mathcal{C}_{2\varrho}, \mathcal{C}_{n\varrho} \rangle) / 2 + \mathcal{S}_{n\xi} (\langle 1, \mathcal{S}_{n\varrho} \rangle + \langle \mathcal{C}_{2\varrho}, \mathcal{S}_{n\varrho} \rangle) / 2, \end{aligned} \quad (\text{B3})$$

and analogously for the other possibilities.

Using the orthogonality relations of cosine and sine functions, $\langle \mathcal{C}_{m\rho}, \mathcal{C}_{n\rho} \rangle = \pi \delta_{nm}$, $\langle \mathcal{S}_{m\rho}, \mathcal{S}_{n\rho} \rangle = \pi \delta_{nm}$, and $\langle \mathcal{S}_{m\rho}, \mathcal{C}_{n\rho} \rangle = \delta_{nm}$, for $m, n \geq 1$, we find

$$\int_0^{2\pi} d\varphi_\varrho \cos^2(\varphi_\varrho) \cos(n\varphi_\xi - n\varphi_\varrho) = \pi \delta_{n0} + \frac{\pi}{2} \cos(2\varphi_\xi) \delta_{n2}, \quad (\text{B4a})$$

$$\int_0^{2\pi} d\varphi_\varrho \sin^2(\varphi_\varrho) \cos(n\varphi_\xi - n\varphi_\varrho) = \pi \delta_{n0} - \frac{\pi}{2} \cos(2\varphi_\xi) \delta_{n2}, \quad (\text{B4b})$$

$$\int_0^{2\pi} d\varphi_\varrho \cos(\varphi_\varrho) \sin(\varphi_\varrho) \cos(n\varphi_\xi - n\varphi_\varrho) = \frac{\pi}{2} \sin(2\varphi_\xi) \delta_{n2}. \quad (\text{B4c})$$

Integral I_{ij} of Eq. (B1a) is then evaluated to

$$I_{ij} = \pi [\delta_{ij} J_0(\xi\rho) - \tau_{ij}(\phi_\xi) J_2(\xi\rho)], \quad (\text{B5})$$

with

$$\tau_{ij}(\phi_\xi) \equiv \begin{bmatrix} \cos(2\phi_\xi) & \sin(2\phi_\xi) \\ \sin(2\phi_\xi) & -\cos(2\phi_\xi) \end{bmatrix}_{ij}. \quad (\text{B6})$$

The integral of Eq. (B1b) is simpler,

$$\begin{aligned}
I_{iz} &= \int_0^{2\pi} \psi_i(\varphi_\varrho) J_0(\xi\varrho) d\varphi_\varrho \\
&\quad + 2 \sum_{n=1}^{\infty} (-i)^n \int_0^{2\pi} \psi_i(\varphi_\varrho) \cos(n\varphi_\xi - n\varphi_\varrho) J_n(\xi\varrho) d\varphi_\varrho.
\end{aligned} \tag{B7}$$

In this case, the integral for $n = 0$ is null, and we need to check only $n \geq 1$,

$$\begin{aligned}
\int_0^{2\pi} d\varphi_\varrho \psi_i(\varphi_\varrho) \cos(n\varphi_\xi - n\varphi_\varrho) &= \mathcal{C}_{n\xi} \langle \psi_i, \mathcal{C}_{n\varrho} \rangle + \mathcal{S}_{n\xi} \langle \psi_i, \mathcal{S}_{n\varrho} \rangle \\
&= \pi \psi_i(\varphi_\xi) \delta_{n1}.
\end{aligned} \tag{B8}$$

The integral is then evaluated to

$$I_{iz} = -2\pi i \psi_i(\phi_\xi) J_1(\xi\rho). \tag{B9}$$

Finally, the integral of Eq. (B1c) is the simplest,

$$\begin{aligned}
I_{zz} &= \int_0^{2\pi} J_0(\xi\varrho) d\varphi_\varrho \\
&\quad + 2 \sum_{n=1}^{\infty} (-i)^n \int_0^{2\pi} \cos(n\varphi_\xi - n\varphi_\varrho) J_n(\xi\varrho) d\varphi_\varrho,
\end{aligned} \tag{B10}$$

because all terms $n \geq 1$ yield zero, and

$$I_{zz} = 2\pi J_0(\xi\rho). \tag{B11}$$

Appendix C: Integrals of Bessel functions

In this Appendix, we provide exact analytical solutions to the integrals that appear in Sec. V. In order to obtain the solutions of the TST terms, we will need the relation

$$\int_0^\infty \frac{\varrho^{\nu+1}}{(\varrho^2 + a^2)^{\mu+1}} J_\nu(\xi\varrho) d\varrho = \frac{\xi^\mu a^{\nu-\mu}}{2^\mu \Gamma(\mu+1)} K_{\nu-\mu}(a\xi), \tag{C1}$$

where $K_\nu(\xi)$ is the modified Bessel function of the second kind, and which comes from the theory of Hankel (or Bessel) transforms [19]. We will also use the transform of the solution of the Bessel equation [22],

$$\int_0^\infty (-\varrho^2) f(\varrho) J_\nu(\xi\varrho) d\varrho = \frac{\partial^2 F_\nu(\xi)}{\partial \xi^2} + \frac{1}{\xi} \frac{\partial F_\nu(\xi)}{\partial \xi} - \frac{\nu^2}{\xi^2} F_\nu(\xi), \tag{C2}$$

where $F_\nu(\xi) \equiv \int_0^\infty f(\varrho) J_\nu(\xi\varrho) d\varrho$.

To calculate

$$\int_0^\infty \frac{\varrho^2}{(\varrho^2 + 1)^5} J_0(\xi\varrho) \varrho d\varrho, \quad (\text{C3})$$

we write it as

$$- \int_0^\infty (-\varrho^2) \frac{\varrho}{(\varrho^2 + 1)^5} J_0(\xi\varrho) d\varrho. \quad (\text{C4})$$

Then we can identify $\mu = 4$ and $\nu = 0$ to insert in Eq. (C1), such that

$$\int_0^\infty \frac{\varrho^2}{(\varrho^2 + 1)^5} J_0(\xi\varrho) \varrho d\varrho = -\frac{\partial^2 F_0^{\text{TST}}(\xi)}{\partial \xi^2} - \frac{1}{\xi} \frac{\partial F_0^{\text{TST}}(\xi)}{\partial \xi}, \quad (\text{C5})$$

with

$$F_0^{\text{TST}}(\xi) = \int_0^\infty \frac{\varrho}{(\varrho^2 + 1)^5} J_0(\xi\varrho) d\varrho = \frac{\xi^4}{2^4 \Gamma(5)} K_4(\xi), \quad (\text{C6})$$

where we used that $K_{-\nu}(\xi) = K_\nu(\xi)$ [23]. Then, using $\frac{d}{d\xi}(\xi^\nu K_\nu(\xi)) = -\xi^\nu K_{\nu-1}(\xi)$ [23], one arrives at

$$\int_0^\infty \frac{\varrho^2}{(\varrho^2 + 1)^5} J_0(\xi\varrho) \varrho d\varrho = \frac{1}{2^4 \Gamma(5)} [2\xi^3 K_3(\xi) - \xi^4 K_2(\xi)], \quad (\text{C7})$$

in which $2^4 \Gamma(5) = 384$.

All other integrals are a direct application of Eq. (C1), where we can use

$$K_{1/2}(\xi) = \sqrt{\frac{\pi}{2\xi}} e^{-\xi}, \quad (\text{C8a})$$

$$K_{3/2}(\xi) = \sqrt{\frac{\pi}{2\xi}} \left(1 + \frac{1}{\xi}\right) e^{-\xi}, \quad (\text{C8b})$$

in the ST ones. Below we list the exact analytical results of all the integrals needed in Sec. V.

1. TST terms

$$\int_0^\infty \frac{\varrho^2}{(\varrho^2 + 1)^5} J_0(\xi\varrho) \varrho d\varrho = \frac{1}{384} [2\xi^3 K_3(\xi) - \xi^4 K_2(\xi)] \quad (\text{C9})$$

$$\int_0^\infty \frac{\varrho^2}{(\varrho^2 + 1)^5} J_2(\xi\varrho) \varrho d\varrho = \frac{1}{384} \xi^4 K_2(\xi) \quad (\text{C10})$$

$$\int_0^\infty \frac{\varrho}{(\varrho^2 + 1)^5} J_1(\xi\varrho) \varrho d\varrho = \frac{1}{384} \xi^4 K_3(\xi) \quad (\text{C11})$$

$$\int_0^\infty \frac{\varrho}{(\varrho^2 + 1)^4} J_1(\xi\varrho) \varrho d\varrho = \frac{1}{48} \xi^3 K_2(\xi) \quad (\text{C12})$$

$$\int_0^\infty \frac{1}{(\varrho^2 + 1)^5} J_0(\xi\varrho)\varrho d\varrho = \frac{1}{384}\xi^4 K_4(\xi) \quad (\text{C13})$$

$$\int_0^\infty \frac{1}{(\varrho^2 + 1)^3} J_0(\xi\varrho)\varrho d\varrho = \frac{1}{8}\xi^2 K_2(\xi) \quad (\text{C14})$$

$$\int_0^\infty \frac{1}{(\varrho^2 + 1)^4} J_0(\xi\varrho)\varrho d\varrho = \frac{1}{48}\xi^3 K_3(\xi) \quad (\text{C15})$$

2. ST terms

$$\int_0^\infty \frac{\varrho}{(\varrho^2 + 1)^{5/2}} J_1(\xi\varrho)\varrho d\varrho = \frac{1}{3}\xi e^{-\xi} \quad (\text{C16})$$

$$\int_0^\infty \frac{1}{(\varrho^2 + 1)^{5/2}} J_0(\xi\varrho)\varrho d\varrho = \frac{1}{3}(1 + \xi)e^{-\xi} \quad (\text{C17})$$

$$\int_0^\infty \frac{1}{(\varrho^2 + 1)^{3/2}} J_0(\xi\varrho)\varrho d\varrho = e^{-\xi} \quad (\text{C18})$$

Appendix D: Derivation of the tensorial contribution to the TERS signal

The goal of this appendix is to derive a compact form for the $\mathcal{I}^{(\eta)}$ functions, defined in Eq. (17), which carry the all the tensorial properties of the TERS scattering of mode η . Using Eq. (47), we can write

$$\begin{aligned} \mathcal{I}^{(A_1)} = |\bar{\alpha}^{(A_1)}|^2 |E_z(\omega)|^2 & \left\{ |g_z^{\text{FF}}|^2 \left| \left(\frac{\alpha_{zz}^{\text{tip}}}{4\pi\epsilon_0} \right)^2 \frac{\pi}{z^4} [h_{xx}(\xi, \varphi_\xi) + h_{yy}(\xi, \varphi_\xi) + \nu h_{zz}(\xi, \varphi_\xi)] \right. \right. \\ & \left. \left. + 2\nu \left(\frac{\alpha_{zz}^{\text{tip}}}{4\pi\epsilon_0} \right) \frac{\pi}{z} a_z(\xi, \varphi_\xi) \right|^2 \right. \\ & \left. + |g_{\parallel}^{\text{FF}}|^2 \left| \frac{\alpha_{zz}^{\text{tip}}}{4\pi\epsilon_0} \right|^2 \frac{\pi^2}{z^2} [|a_x(\xi, \varphi_\xi)|^2 + |a_y(\xi, \varphi_\xi)|^2] \right\}, \quad (\text{D1a}) \end{aligned}$$

$$\begin{aligned} \mathcal{I}^{(E_{2g,x})} = |\bar{\alpha}^{(E_{2g})}|^2 |E_z(\omega)|^2 & \left\{ |g_z^{\text{FF}}|^2 \left| \frac{\alpha_{zz}^{\text{tip}}}{4\pi\epsilon_0} \right|^4 \frac{\pi^2}{z^8} |h_{xy}(\xi, \varphi_\xi) + h_{yx}(\xi, \varphi_\xi)|^2 \right. \\ & \left. + |g_{\parallel}^{\text{FF}}|^2 \left| \frac{\alpha_{zz}^{\text{tip}}}{4\pi\epsilon_0} \right|^2 \frac{\pi^2}{z^2} [|a_x(\xi, \varphi_\xi)|^2 + |a_y(\xi, \varphi_\xi)|^2] \right\}, \quad (\text{D1b}) \end{aligned}$$

$$\begin{aligned} \mathcal{I}^{(E_{2g,y})} = |\bar{\alpha}^{(E_{2g})}|^2 |E_z(\omega)|^2 & \left\{ |g_z^{\text{FF}}|^2 \left| \frac{\alpha_{zz}^{\text{tip}}}{4\pi\epsilon_0} \right|^4 \frac{\pi^2}{z^8} |h_{xx}(\xi, \varphi_\xi) - h_{yy}(\xi, \varphi_\xi)|^2 \right. \\ & \left. + |g_{\parallel}^{\text{FF}}|^2 \left| \frac{\alpha_{zz}^{\text{tip}}}{4\pi\epsilon_0} \right|^2 \frac{\pi^2}{z^2} [|a_x(\xi, \varphi_\xi)|^2 + |a_y(\xi, \varphi_\xi)|^2] \right\}. \quad (\text{D1c}) \end{aligned}$$

Crucially, we have to work on the angular dependence of $\mathcal{I}^{(n)}$, that is, the dependence on variable φ_ξ . The first simplification we do in this sense is that, using Eq. (40), one can write

$$\begin{aligned} |a_x(\xi, \varphi_\xi)|^2 + |a_y(\xi, \varphi_\xi)|^2 &= 4\xi^2 e^{-2\xi} [|\psi_x(\varphi_\xi)|^2 + |\psi_y(\varphi_\xi)|^2] \\ &= 4\xi^2 e^{-2\xi}, \end{aligned} \quad (\text{D2})$$

meaning that the sample plane polarization in the ST contribution is independent of φ_ξ for all modes. We also note that, from Eq. (35) and (40) all the z contribution in Eq. (D1) is also independent of φ_ξ ,

$$h_{zz}(\xi, \varphi_\xi) = 2 \left[\frac{9}{384} \xi^4 K_4(\xi) - \frac{6}{48} \xi^3 K_3(\xi) + \frac{1}{8} \xi^2 K_2(\xi) \right], \quad (\text{D3a})$$

$$a_z(\xi, \varphi_\xi) = 2\xi e^{-\xi}. \quad (\text{D3b})$$

We are left with

$$h_{xx}(\xi, \varphi_\xi) + h_{yy}(\xi, \varphi_\xi) = 2 \frac{9}{384} [2\xi^3 K_3(\xi) - \xi^4 K_2(\xi)], \quad (\text{D4a})$$

$$h_{xy}(\xi, \varphi_\xi) + h_{yx}(\xi, \varphi_\xi) = -2 \sin(2\varphi_\xi) \frac{9}{384} \xi^4 K_2(\xi), \quad (\text{D4b})$$

$$h_{xx}(\xi, \varphi_\xi) - h_{yy}(\xi, \varphi_\xi) = -2 \cos(2\varphi_\xi) \frac{9}{384} \xi^4 K_2(\xi), \quad (\text{D4c})$$

where we used the definition of $\tau_{ij}(\varphi_\xi)$, Eq. (34).

Substitution of the above equations in Eq. (D1) yields

$$\begin{aligned} \mathcal{I}^{(A_1)} = |\bar{\alpha}^{(A_1)}|^2 |E_z(\omega)|^2 &\left\{ |g_z^{\text{FF}}|^2 \left| \left(\frac{\alpha_{zz}^{\text{tip}}}{4\pi\epsilon_0} \right)^2 \frac{\pi}{z^4} \left[\frac{3}{32} \xi^3 K_3(\xi) - \frac{3}{64} \xi^4 K_2(\xi) \right] \right. \right. \\ &+ \nu \left(\frac{\alpha_{zz}^{\text{tip}}}{4\pi\epsilon_0} \right)^2 \frac{\pi}{z^4} \left[\frac{3}{64} \xi^4 K_4(\xi) - \frac{1}{4} \xi^3 K_3(\xi) + \frac{1}{4} \xi^2 K_2(\xi) \right] \\ &+ 4\nu \left(\frac{\alpha_{zz}^{\text{tip}}}{4\pi\epsilon_0} \right) \frac{\pi}{z} \xi e^{-\xi} \left. \right|^2 \\ &+ 4 |g_{\parallel}^{\text{FF}}|^2 \left| \frac{\alpha_{zz}^{\text{tip}}}{4\pi\epsilon_0} \right|^2 \frac{\pi^2}{z^2} \xi^2 e^{-2\xi} \left. \right\}, \end{aligned} \quad (\text{D5a})$$

$$\begin{aligned} \mathcal{I}^{(E_{2g}, x)} = |\bar{\alpha}^{(E_{2g})}|^2 |E_z(\omega)|^2 &\left\{ 4 |g_z^{\text{FF}}|^2 \left| \frac{\alpha_{zz}^{\text{tip}}}{4\pi\epsilon_0} \right|^4 \frac{\pi^2}{z^8} \sin^2(2\varphi_\xi) \left(\frac{3}{128} \right)^2 \xi^8 [K_2(\xi)]^2 \right. \\ &+ 4 |g_{\parallel}^{\text{FF}}|^2 \left| \frac{\alpha_{zz}^{\text{tip}}}{4\pi\epsilon_0} \right|^2 \frac{\pi^2}{z^2} \xi^2 e^{-2\xi} \left. \right\}, \end{aligned} \quad (\text{D5b})$$

$$\mathcal{I}^{(E_{2g},y)} = |\bar{\alpha}^{(E_{2g})}|^2 |E_z(\omega)|^2 \left\{ 4 |g_z^{\text{FF}}|^2 \left| \frac{\alpha_{zz}^{\text{tip}}}{4\pi\epsilon_0} \right|^4 \frac{\pi^2}{z^8} \cos^2(2\varphi_\xi) \left(\frac{3}{128} \right)^2 \xi^8 [K_2(\xi)]^2 + 4 |g_{\parallel}^{\text{FF}}|^2 \left| \frac{\alpha_{zz}^{\text{tip}}}{4\pi\epsilon_0} \right|^2 \frac{\pi^2}{z^2} \xi^2 e^{-2\xi} \right\}. \quad (\text{D5c})$$

Having calculated $\mathcal{I}^{(n)}$, we can now calculate $\mathcal{J}^{(n)}(\xi; z) \equiv \int_0^{2\pi} \mathcal{I}^{(n)}(\xi, \varphi_\xi; z) d\varphi_\xi$, which evaluates to

$$\begin{aligned} \mathcal{J}^{(A_1)}(\xi; z) = 2\pi |\bar{\alpha}^{(A_1)}|^2 |E_z(\omega)|^2 & \left\{ |g_z^{\text{FF}}|^2 \left| \left(\frac{\alpha_{zz}^{\text{tip}}}{4\pi\epsilon_0} \right)^2 \frac{2\pi}{z^4} \left(\frac{9}{384} \right) [2\xi^3 K_3(\xi) - \xi^4 K_2(\xi)] \right. \right. \\ & + \nu \left(\frac{\alpha_{zz}^{\text{tip}}}{4\pi\epsilon_0} \right)^2 \frac{2\pi}{z^4} \left[\frac{9}{384} \xi^4 K_4(\xi) - \frac{6}{48} \xi^3 K_3(\xi) + \frac{1}{8} \xi^2 K_2(\xi) \right] \\ & + 2\nu \left(\frac{\alpha_{zz}^{\text{tip}}}{4\pi\epsilon_0} \right) \frac{2\pi}{z} \xi e^{-\xi} \left. \right|^2 \\ & + |g_{\parallel}^{\text{FF}}|^2 \left| \left(\frac{\alpha_{zz}^{\text{tip}}}{4\pi\epsilon_0} \right) \frac{2\pi}{z} \xi e^{-\xi} \right|^2 \left. \right\}, \quad (\text{D6a}) \end{aligned}$$

$$\begin{aligned} \mathcal{J}^{(E_{2g},x)}(\xi; z) &= \mathcal{J}^{(E_{2g},y)}(\xi; z) \\ &= 2\pi |\bar{\alpha}^{(E_{2g})}|^2 |E_z(\omega)|^2 \left\{ \frac{1}{2} |g_z^{\text{FF}}|^2 \left| \left(\frac{\alpha_{zz}^{\text{tip}}}{4\pi\epsilon_0} \right)^2 \frac{2\pi}{z^4} \left(\frac{3}{128} \right) \xi^4 K_2(\xi) \right|^2 \right. \\ & \quad \left. + |g_{\parallel}^{\text{FF}}|^2 \left| \left(\frac{\alpha_{zz}^{\text{tip}}}{4\pi\epsilon_0} \right) \frac{2\pi}{z} \xi e^{-\xi} \right|^2 \right\}. \quad (\text{D6b}) \end{aligned}$$

REFERENCES

- [1] M. Cardona, ed., *Light scattering in solids I* (Springer-Verlag, Berlin, 1983).
- [2] N. Bloembergen, *Nonlinear optics*, 4th ed. (World Scientific, New York, 1996).
- [3] L. Novotny and B. Hecht, *Principles of nano-optics*, 2nd ed. (Cambridge University Press, Cambridge, 2012).
- [4] S. Kawata and V. M. Shalaev, eds., *Tip enhancement* (Elsevier, Amsterdam, 2007).
- [5] A. Jorio, R. Nadas, A. G. Pereira, C. Rabelo, A. C. Gadelha, T. L. Vasconcelos, W. Zhang, Y. Miyata, R. Saito, M. D. D. Costa, and L. G. Cançado, Nano-Raman spectroscopy of 2D materials, *2D Mater.* **11**, 033003 (2024).
- [6] Y.-F. Bao, M.-Y. Zhu, X.-J. Zhao, H.-X. Chen, X. W. Wang, and B. Ren, Nanoscale chemical characterization of materials and interfaces by tip-enhanced Raman spectroscopy, *Chem. Soc. Rev.* 10.1039/D4CS00588K (2024).

- [7] R. Beams, L. G. Cançado, S.-H. Oh, A. Jorio, and L. Novotny, Spatial coherence in near-field Raman scattering, *Phys. Rev. Lett.* **113**, 186101 (2014).
- [8] R. Nadas, R. Corrêa, L. G. Cançado, and A. Jorio, Tip-enhanced Raman spectroscopy coherence length of 2D materials: An application to graphene, *Phys. Status Solidi B* **262**, 2400287 (2025).
- [9] R. S. Alencar, C. Rabelo, H. L. S. Miranda, T. L. Vasconcelos, B. S. Oliveira, A. Ribeiro, B. C. Públio, J. Ribeiro-Soares, A. G. S. Filho, L. G. Cançado, and A. Jorio, Probing spatial phonon correlation length in post-transition metal monochalcogenide GaS using tip-enhanced Raman spectroscopy, *Nano Lett.* **19**, 7357 (2019).
- [10] L. G. Cançado, R. Beams, A. Jorio, and L. Novotny, Theory of spatial coherence in near-field Raman scattering, *Phys. Rev. X* **4**, 031054 (2014).
- [11] B. C. Publio, B. S. Oliveira, C. Rabelo, H. Miranda, T. L. Vasconcelos, A. Jorio, and L. G. Cançado, Inclusion of the sample-tip interaction term in the theory of tip-enhanced Raman spectroscopy, *Phys. Rev. B* **105**, 235414 (2022).
- [12] M. Jin, W. Zheng, Y. Ding, Y. Zhu, W. Wang, and F. Huang, Raman tensor of van der Waals MoSe₂, *J. Phys. Chem. Lett.* **11**, 4311 (2020).
- [13] F. R. Pratama, M. S. Ukhtary, and R. Saito, Non-vertical optical transition in near-field enhanced spectroscopy of graphene, *J. Phys.: Condens. Matter* **31**, 265701 (2019).
- [14] We do not use repeated index summation convention because it may get ambiguous later.
- [15] P.-H. Tan, ed., *Raman spectroscopy of Two-dimensional materials* (Springer Nature, Singapore, 2019).
- [16] K.-D. Park, O. Khatib, V. Kravtsov, G. Clark, X. Xu, and M. B. Raschke, Hybrid tip-enhanced nanospectroscopy and nanoimaging of monolayer WSe₂ with local strain control, *Nano Lett.* **16**, 2621 (2016).
- [17] A. Jorio, R. Saito, G. Dresselhaus, and M. S. Dresselhaus, *Raman Spectroscopy in Graphene Related Systems* (Wiley-VCH Verlag, Weinheim, 2012).
- [18] Y. Zhao, X. Luo, H. Li, J. Zhang, P. T. Araujo, C. K. Gan, J. Wu, H. Zhang, S. Y. Quek, M. S. Dresselhaus, and Q. Xiong, Interlayer breathing and shear modes in few-trilayer MoS₂ and WSe₂, *Nano Lett.* **13**, 1007 (2013).
- [19] R. Piessens, The Hankel transform, in *The Transforms and Applications Handbook*, edited by A. D. Poularikas (CRC Press LLC, Boca Raton, 2000) 2nd ed.

- [20] H. Miranda, V. Monken, J. a. L. E. Campos, T. L. Vasconcelos, C. Rabelo, B. S. Archanjo, C. M. Almeida, S. Grieger, C. Backes, A. Jorio, and L. Gustavo Cançado, Establishing the excitation field in tip-enhanced Raman spectroscopy to study nanostructures within two-dimensional systems, *2D Mater.* **10**, 015002 (2022).
- [21] A. Cuyt, V. B. Petersen, B. Verdonk, H. Waadeland, and W. B. Jones, *Handbook of Continued Fractions for Special Functions* (Springer, 2008).
- [22] B. Davies, *Integral transforms and their applications*, 3rd ed. (Springer-Verlag, New York, 2002).
- [23] F. E. Relton, *Applied Bessel functions* (Dover Publications, New York, 1965).
- [24] L. G. Cançado, A. Jorio, A. Ismach, E. Joselevich, A. Hartschuh, and L. Novotny, Mechanism of near-field Raman enhancement in one-dimensional systems, *Phys. Rev. Lett.* **103**, 186101 (2009).
- [25] J. E. Guimarães, R. Nadas, R. Alves, W. Zhang, T. Endo, K. Watanabe, T. Taniguchi, R. Saito, Y. Miyata, B. R. A. Neves, and A. Jorio, Nano-Raman spectroscopy figure of merit and chemical analysis of contaminations in single-layer MoSe₂, *ACS Nano* **19**, 35438 (2025).
- [26] J. D. Jackson, *Classical Electrodynamics*, 3rd ed. (John Wiley & Sons, New York, 1999).
- [27] R. B. Nadas, A. C. Gadelha, T. C. Barbosa, C. Rabelo, T. de Lourenço e Vasconcelos, V. Monken, A. V. R. Portes, K. Watanabe, T. Taniguchi, J. C. Ramirez, L. C. Campos, R. Saito, L. G. Cançado, and A. Jorio, Spatially coherent tip-enhanced raman spectroscopy measurements of electron–phonon interaction in a graphene device, *Nano Lett.* **23**, 8827 (2023).
- [28] A. R. Neto, C. Rabelo, L. G. Cançado, M. Engel, M. Steiner, and A. Jorio, Protocol and reference material for measuring the nanoantenna enhancement factor in tip-enhanced Raman spectroscopy, in *2019 4th International Symposium on Instrumentation Systems, Circuits and Transducers (INSCIT)* (2019) pp. 1–6.